CM² MAGAZINE

第 60 期

南方科技大学海洋磁学中心主编

https://cm2.sustech.edu.cn/

创刊词

海洋是生命的摇篮，是文明的纽带。地球上最早的生命诞生于海洋，海洋里的生命最终进化成了人类，人类的文化融合又通过海洋得以实现。人因海而兴。

人类对海洋的探索从未停止。从远古时代美丽的神话传说，到麦哲伦的全球航行，再到现代对大洋的科学钻探计划，海洋逐渐从人类敬畏崇拜幻想的精神寄托演变成可以开发利用与科学研究的客观存在。其中，上个世纪与太空探索同步发展的大洋科学钻探计划将人类对海洋的认知推向了崭新的纬度：深海（deep sea）与深时（deep time）。大洋钻探计划让人类知道，奔流不息的大海之下，埋藏的却是亿万年的地球历史。它们记录了地球板块的运动，从而使板块构造学说得到证实；它们记录了地球环境的演变，从而让古海洋学方兴未艾。

在探索海洋的悠久历史中，从大航海时代的导航，到大洋钻探计划中不可或缺的磁性地层学，磁学发挥了不可替代的作用。这不是偶然，因为从微观到宏观，磁性是最基本的物理属性之一，可以说，万物皆有磁性。基于课题组的学科背景和对海洋的理解，我们对海洋的探索以磁学为主要手段，海洋磁学中心因此而生。

海洋磁学中心，简称 CM^2，一为其全名“Centre for Marine Magnetism”的缩写，另者恰与爱因斯坦著名的质能方程 $E = MC^2$ 对称，借以表达我们对科学巨匠的敬仰和对科学的不懈追求。

然而科学从来不是单打独斗的产物。我们以磁学为研究海洋的主攻利器，但绝不仅限于磁学。凡与磁学相关的领域均是我们关注的重点。为了跟踪反映国内外地球科学特别是与磁学有关的地球科学领域的最新研究进展，海洋磁学中心特地主办 CM^2 Magazine，以期与各位地球科学工作者相互交流学习、合作共进！

“海洋孕育了生命，联通了世界，促进了发展”。 21 世纪是海洋科学的时代，由陆向海，让我们携手迈进中国海洋科学的黄金时代。

目 录

文献速递

1. Li 同位素测量硅质岩浆喷发时挥发组分丢失的时间尺度 1
2. 世纪营地冰盖 1.4 km 下沉积物记录格陵兰百万年的植被和冰期历史 3
3. 南美洲 Parana 盆地东北部的 Illawarra 倒转开始时间和二叠纪中-晚期磁性地层学 7
4. 应用赤铁矿重建科罗拉多高原晚三叠纪水文气候 11
5. 蒸发岩风化与沉积是调控长时间尺度气候的控制因素 14
6. 东特提斯最东端中生代地壳生长:来自印度尼西亚苏门答腊花岗岩的 Hf 同位素证据 16
7. 航磁资料对 Knipovich 洋脊扩张演化的新解释 19
8. 珠江口盆地白云凹陷后裂陷期海底火山杂岩与断裂活动：对南海北部破裂层序的新认识 21
9. 季风降雨氧同位素组成的记录者：中国黄土微松藻 25
10. 东白令海晚第四纪海冰和沉积物氧化还原条件对北太平洋中深水通风和大西洋—太平洋跷跷板机制的影响 29
11. 低对流层过程，控制全球平均降水率 35
12. 热带石笋的 QDM 高分辨率环境磁学研究 38
13. 多样品平行 pTRM 差异法测定小高加索地区上新世火山岩古强度，并与 Thellier - Thellier 和 IZZI 法结果比较 40
14. 地球上最深海沟沉积物中微生物碳的高速周转 44

1. Li 同位素测量硅质岩浆喷发时挥发组分丢失的时间尺度

翻译人：冯婉仪 fengwy@sustech.edu.cn

Neukampf J, Ellis B S, Laurent O, et al. ***Time scales of syneruptive volatile loss in silicic magmas quantified by Li isotopes*** *[J]. Geology, 2021, 49:125-129.*

https://doi.org/10.1130/G47764.1

摘要：大多数具有爆发力的硅质火山在两次喷发之间都要休眠数千年。从休眠状态到喷发状态转变的时间是解读监测信号和提高生活在活火山附近的人们安全的关键。我们利用一种新技术解决了这个问题，该技术基于来自美国爱达荷州和怀俄明州黄石火山系统的 Mesa Falls 凝灰岩中斜长石晶体的锂同位素（δ^7Li）和元素浓度剖面，将挥发分脱气作用限定在喷发前几十分钟的最短时间尺度内发生。在这短暂的时间内，从晶体核部到边部，Li 含量下降了 4-10 倍，同时 δ^7Li 增加了 10‰，这反映了斜长石核部与贫 Li 熔体之间的由扩散作用驱动的平衡。在这项研究中获得的新的时间尺度显示了岩浆中的挥发组分在岩浆喷发同时快速变化的潜力。

ABSTRACT: Most explosive, silicic volcanoes spend thousands of years in repose between eruptive events. The timing of the switch from repose to eruption is key to interpreting monitoring signals and improving the safety of people living close to active volcanoes. We addressed this question using a novel technique based on lithium isotopic (δ^7Li) and elemental concentration profiles within plagioclase crystals from the Mesa Falls Tuff of the Yellowstone volcanic system (Idaho and Wyoming, USA), constraining volatile degassing to occur on minimum time scales of tens of minutes prior to eruption. During this ephemeral time, Li abundances drop by a factor of four to 10 from crystal cores to rims, accompanied by an increase in δ^7Li of as much as 10‰, reflecting diffusion-driven equilibration between plagioclase cores and outgassed, Li-poor melt. New times scales obtained in this study show the potential for rapid syneruptive changes in the volatile inventory of magmas.

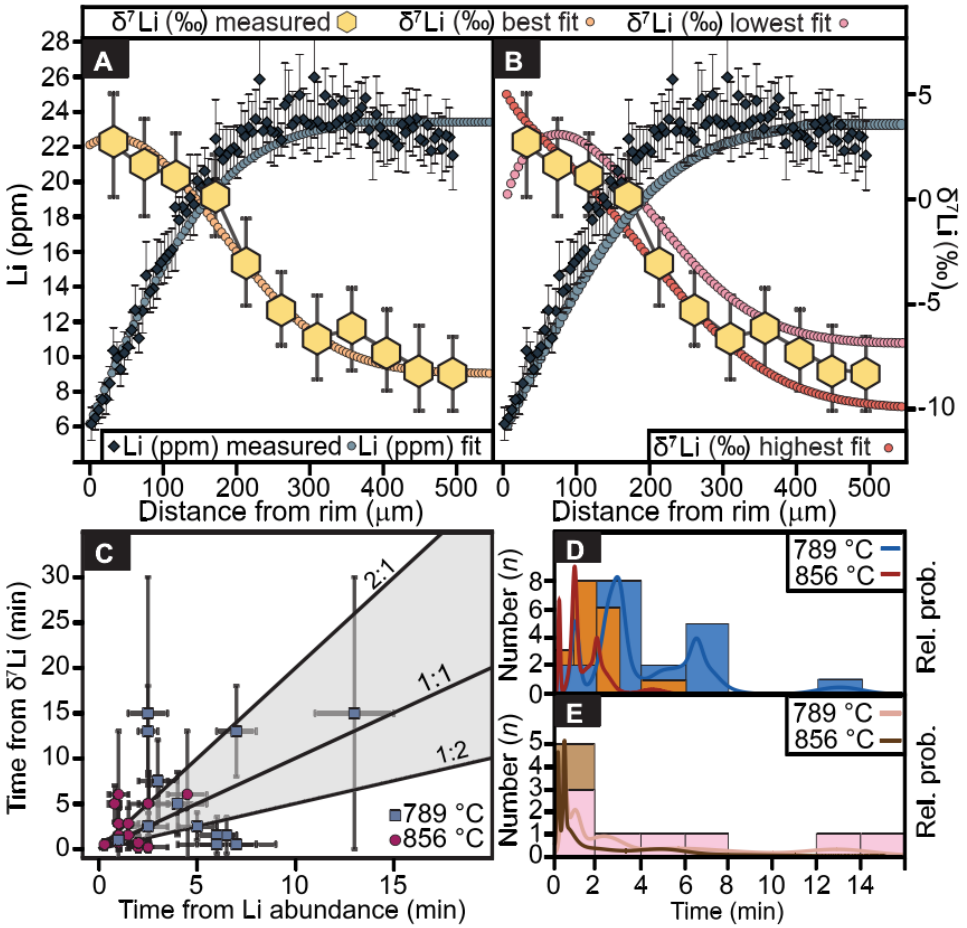

Figure 1. Example of one-dimensional Li diffusion model for Mesa Falls Tuff plagioclase (Yellowstone volcanic system, Idaho and Wyoming, USA). (A) Representative diffusion profile with measured (blue diamonds) concentration profile and its modeled best fit (blue circles), in situ measured δ^7Li data (yellow hexagons), and best fit for δ^7Li profile (orange circles). (B) Profiles shown in A with boundary conditions set to highest (red) and lowest (pink) isotopic value within analytical error. (C) Comparison of time scales obtained by diffusion modeling of Li concentration (Li abundance) and isotope (δ^7Li) profiles. Blue squares represent time scales at 789 °C, and red circles refer to time scales at 856 °C. Errors are provided as dark gray error bars. Lines labeled 1:1, 2:1, and 1:2 and the gray shaded area indicate the field of best agreement between time scales obtained for Li concentration and isotope profiles. (D) Time scales obtained from Li concentration profiles (n = 18) shown as lines at 789 °C (blue) and 856 °C (red) for their relative probability (Rel. prob.). Histogram (789 °C in blue, 856 °C in orange) shows distribution of time scales. (E) Time scales obtained from all eight (two profiles in the same crystal) analyzed δ^7Li profiles at 789 °C (pink) and at 856 °C (brown). Histogram (789 °C in pink, 856 °C in brown) shows distribution of the time scales.

2. 世纪营地冰盖 1.4km 下沉积物记录格陵兰百万年的植被和冰期历史

翻译人：蒋晓东 jiangxd@sustech.edu.cn

Christ A J, Bierman P R, Schaefer J M, et al. ***A multimillion-year-old record of Greenland vegetation and glacial history preserved in sediment beneath 1.4 km of ice at Camp Century*** *[J]. Proceedings of the National Academy of Sciences, 2021, 118, e2021442118.*

https://doi.org/10.1073/pnas.2021442118

摘要: 理解格陵兰冰盖历史对评估该地区对气候变暖以及海平面上升的敏感性具有至关重要的意义。然而，当前对于对格陵兰末次间冰期之前的历史并不清楚。大多数的相关认知主要依据海洋沉积物，但这是过去冰盖事件和演化行为的间接记录。冰川下的沉积物和岩石为格陵兰冰盖在更新世期间的行为提供了陆地证据。基于 1966 年在世纪营地冰芯下获取的沉积物，本研究使用了多种方法来重建格陵兰冰盖历史，主要包括更新世时期在格陵兰西北地区冰川和植被的地层记录。孔隙冰中增强的稳定同位素表明低海拔的沉积，同时暗示冰盖的缺失。沉积物中的植物化石和生物标志物表明冰盖下保存的间冰期的古生态系统。宇宙射线产生的 $^{26}Al/^{10}Be$ 和冷发光数据表明最底下埋藏的沉积物年龄在 3.2 ± 0.4 Ma 到 0.7 或 1.4 Ma 之间。这些独特的沉积物记录了至少两期无冰且有覆盖植被的事件，这两期事件随后都发生了冰川作用。更低处的沉积物来自于早更新世格陵兰冰盖扩张的产物。最上部沉积物与来自格陵兰中部基岩的 $^{26}Al/^{10}Be$ 比值十分吻合，表明在格陵兰大范围中类似的冰盖历史。本研究认为格陵兰冰盖在更新世大多时期持续稳定，但自 1.1 Ma 以来至少存在一次消融和重塑。

ABSTRACT: Understanding the history of the Greenland Ice Sheet (GrIS) is critical for determining its sensitivity to warming and contribution to sea level; however, that history is poorly known before the last interglacial. Most knowledge comes from interpretation of marine sediment, an indirect record of past ice-sheet extent and behavior. Subglacial sediment and rock, retrieved at the base of ice cores, provide terrestrial evidence for GrIS behavior during the Pleistocene. Here, we use multiple methods to determine GrIS history from subglacial sediment at the base of the Camp Century ice core collected in 1966. This material contains a stratigraphic record of glaciation

and vegetation in northwestern Greenland spanning the Pleistocene. Enriched stable isotopes of pore-ice suggest precipitation at lower elevations implying ice-sheet absence. Plant macrofossils and biomarkers in the sediment indicate that paleo-ecosystems from previous interglacial periods are preserved beneath the GrIS. Cosmogenic $^{26}Al/^{10}Be$ and luminescence data bracket the burial of the lower-most sediment between <3.2 ± 0.4 Ma and >0.7 to 1.4 Ma. In the upper-most sediment, cosmogenic $^{26}Al/^{10}Be$ data require exposure within the last 1.0 ± 0.1 My. The unique subglacial sedimentary record from Camp Century documents at least two episodes of ice-free, vegetated conditions, each followed by glaciation. The lower sediment derives from an Early Pleistocene GrIS advance. $^{26}Al/^{10}Be$ ratios in the upper-most sediment match those in subglacial bedrock from central Greenland, suggesting similar ice-cover histories across the GrIS. We conclude that the GrIS persisted through much of the Pleistocene but melted and reformed at least once since 1.1 Ma.

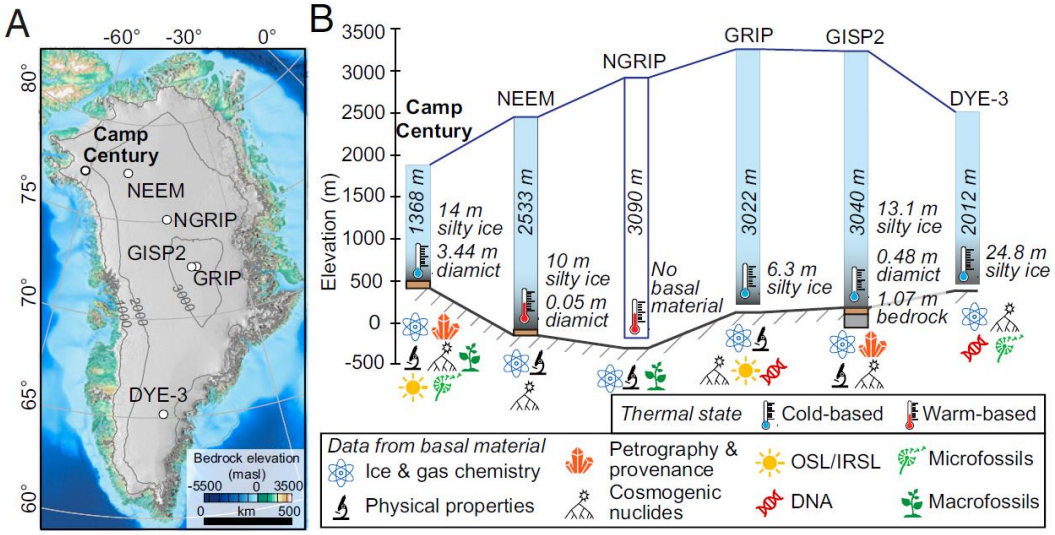

Figure 1. Greenland ice cores and basal materials. (A) Ice core locations (circles) shown with the bedrock topography and ice surface 1,000 m elevation contours (light gray). (B) Ice core glacier ice thickness (to scale) above the bedrock elevation (dark gray line), basal material thickness (exaggerated), and analyses of basal materials (symbols).

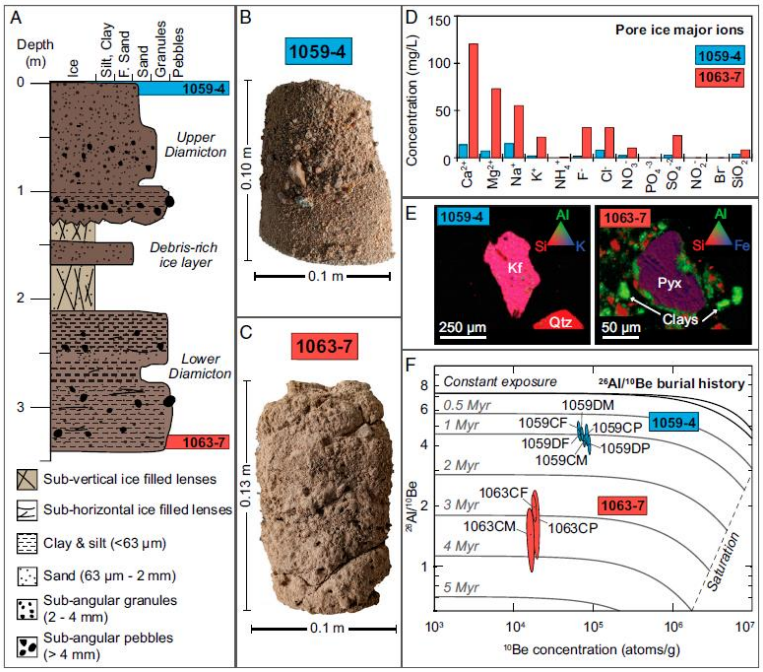

Figure 2. Camp Century basal sediment stratigraphy, weathering, and cosmogenic nuclide results. (A) Sediment description showing sample intervals. Core sample photographs of (B) 1059-4 and (C) 1063-7. (D) Pore-ice major ion chemistry and (E) representative SEM-EDS analysis of mineralogy of the diamictons; Kf, potassium feldspar; Qtz, quartz; Pyx, pyroxene. (F) ^{26}Al and ^{10}Be two-isotope plot showing constant surface exposure (black line) and burial isochrones (light gray) created using ref. 60.

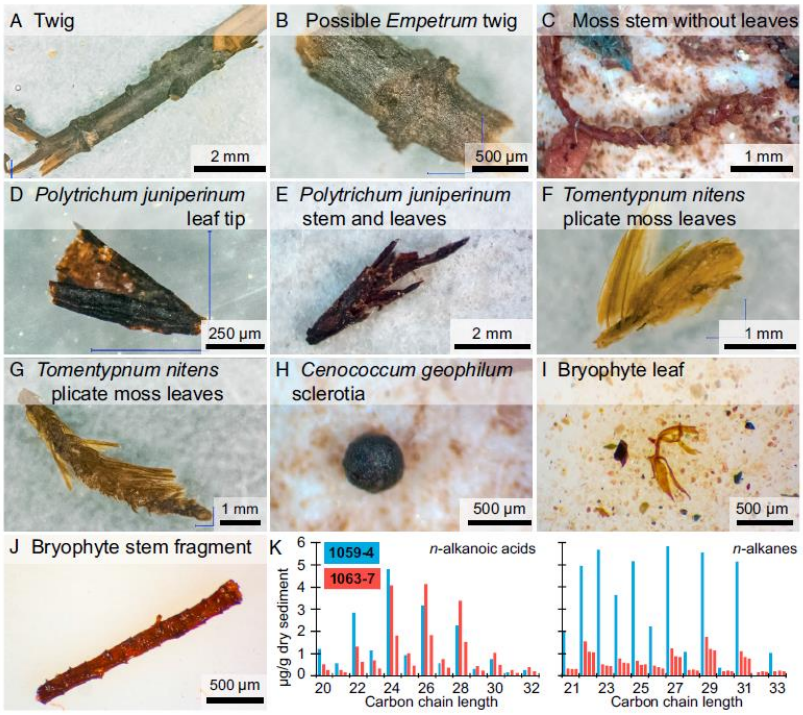

Figure 3. Macrofossil micrographs and leaf wax concentrations. Micrographs of macrofossils recovered in (A–H) the upper diamicton and in (I–J) the lower diamicton. (K) Leaf wax concentrations of n-alkanoic acids and alkanes; multiple columns correspond to replicate analyses.

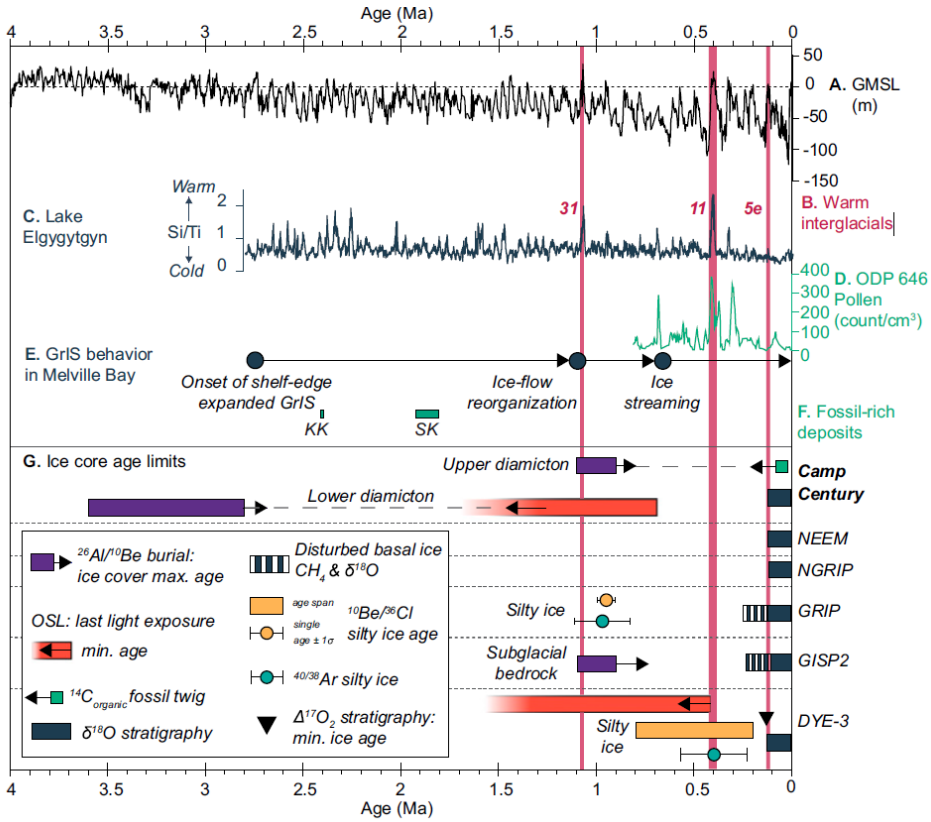

Figure 4. Paleoclimate and Greenland ice-core age constraints since 4 Ma. (A) Global mean sea level; the dashed black line marks the present (37). (B) Pleistocene superinterglacials since 1.1 Ma (pink columns). (C) Si/Ti paleotemperature proxy from Lake El'gygytgyn, Siberia (38). (D) Total minus bisaccate pollen concentration counts in Ocean Drilling Program Site 646, Labrador Sea (3). (E) Changes in GrIS behavior in Melville Bay, west Greenland (6); (F) Green boxes: fossiliferous deposits; KK, Kap København; SK, Store Koldewey (7, 8). (G) Age constraints on materials from Camp Century and other Greenland ice cores (9,10, 12, 20, 23). The dashed gray line shows bounding age constraints for the Camp Century subglacial sediment.

3. 南美洲 Parana 盆地东北部的 Illawarra 倒转开始时间和二叠纪中-晚期磁性地层学

翻译人:李园洁 liyj3@sustech.edu.cn

Aragão M, Scardia G, ***Middle－Late Permian Magnetostratigraphy and the onset of the Illawarra Reversals in the northeastern Parana Basin, South America****[J]. Geophysical Journal International,2021,225(2): 860－871.*

https://doi.org/10.1093/gji/ggab011

摘要：最近汇总的伊拉瓦拉(Illawarra)倒转表明开始时间 (265 Ma vs. 269 Ma) 和地磁极性模式存在不同观点，使得二叠纪中期-晚期的地磁极性年表的建立存在困难。巴拉那 (Parana) 盆地保存有 7 km 厚古生代到中生代的不连续的沉积序列，包括冈瓦纳 1 个从晚石炭纪持续到三叠纪或侏罗纪的超级序列。本文中作者展现一个 300 m 长岩芯的中上二叠统部分的磁性地层学结果。NRM 退磁结果揭示两种磁性叠加，归因于巴拉那布容期和早白垩纪的大火成岩省侵入。稳定的双极性的特征剩磁在温度高于 450 ℃可独立出，表明主要为碎屑剩磁，是在沉积物沉积过程中或刚结束之后获得的。前人文献中的火山锆石的 U-Pb 定年可提供年龄约束。在 Kiaman 超时最上部共识别出 8 个极性倒转，其中最下方的极性带（110 米厚）可以和 Kiaman Superchron 对比。上覆 Illawarra 由负极性带占主导，中间有一层 4-5m 厚的正极性部分。这种模式与 Karoo 盆地和其他二叠纪年表的 Illawarra 序列一致。Illawarra 倒转开始时间为 270 Ma，与 Karoo 盆地的 269 Ma 比较接近。结合磁性地层学和年代学将 Parana 盆地东北部的 Passa Dois Group 的沉积速率定为~8 m/Myr，表明 Serra Alta 和 Teresina Formations 的年龄分别为 279-274 Ma 和 274-254 Ma。

ABSTRACT：Recent compilations of the Illawarra Reversals show remarkable differences in the onset age (265 Ma versus 269 Ma) and the magnetic polarity pattern, hampering the establishment of a reference geomagnetic timescale for the Middle-Late Permian. The Parana Basin hosts a 7-km-thick, discontinuous sedimentary succession spanning the Palaeozoic to the Mesozoic, including the Gondwana 1 supersequence which extends from Late Carboniferous to the Triassic or Jurassic. We provide the magnetostratigraphy of the middle and upper Permian part of this sequence of a ca. 300-

m-long core, pertaining to the Passa Dois Group and the Piramboia Formation. Sample demagnetization of NRM revealed two magnetic overprints ascribed to the Brunhes chron and to the emplacement of Parana Large Igneous Province in the Early Cretaceous, respectively. Stable, dual polarity characteristic components (ChRM) were isolated at temperatures higher than 450 ℃ and interpreted as a primary detrital magnetic remanence (DRM), acquired during or soon after sediment deposition. Available U-Pb dating on volcanic zircons from the literature provided independent chronologic constraints for our magnetostratigraphy. A total of 8 reverse polarity intervals were identified, the lowermost of which (up to 110 m thick) correlates to the Kiaman Superchron. The overlying Illawarra is dominated by a reverse polarity magnetization with thin (4-5 m thick) normal polarity intervals. This pattern agrees with the Illawarra sequence from the Karoo Basin and other proposed timescales for the Permian. The onset of the Illawarra reversals is interpolated to ca. 270 Ma, close to the age of 269 Ma from the Karoo Basin. Combined magnetostratigraphy and geochronology yielded sediment accumulation rates of ca. 8 m Myr^{-1} for the Passa Dois Group in the northeastern (marginal) sector of the Parana Basin, indicating that Serra Alta and Teresina Formations span 279-274 Ma and 274-254 Ma, respectively.

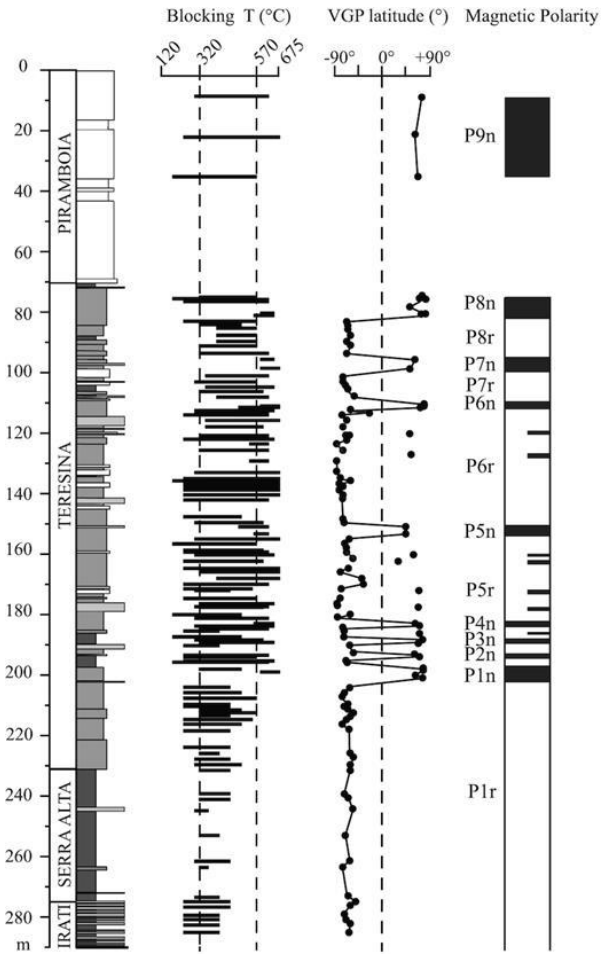

Figure 1. Lithology, C-component blocking temperature spectra, VGP latitudes and magnetic polarities of FP-12-SP. Black (white) rectangles represent normal (reverse) polarities.

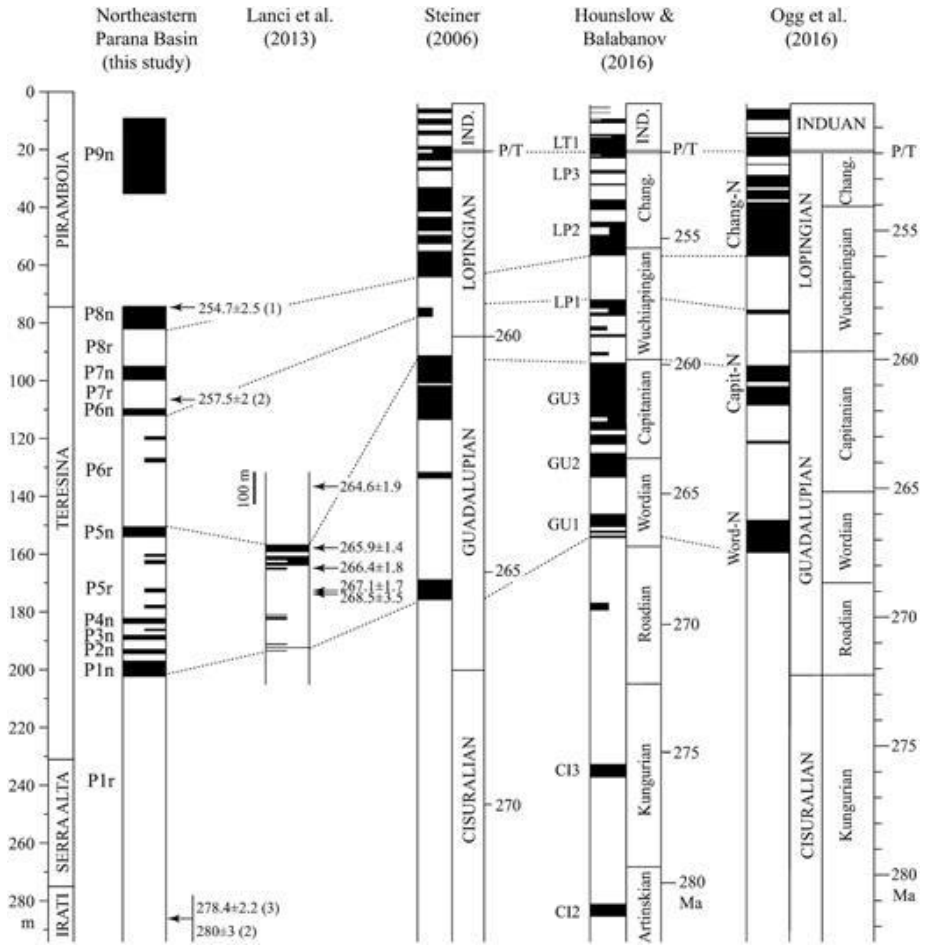

Figure 2. Comparison of FP-12-SP magnetostratigraphy with Karoo Basin (Lanci et al. 2013) and geomagnetic polarity timescales from Steiner (2006), Hounslow & Balabanov (2016), and Ogg et al. (2016). Each column, numerical ages and stages are presented according to their original paper. This paper tentatively aligned the columns by the Permian–Triassic boundary. U-Pb ages: (1) Tohver et al. (2012) (metamorphic zircon); (2) Rocha-Campos et al. (2019); (3) Santos et al. (2006) (volcanic zircon). Black (white) represents normal (reverse) polarities..

4. 应用赤铁矿重建科罗拉多高原晚三叠纪水文气候

翻译人：张琪 zhangq7@sustech.edu.cn

Lepre, J C, Olsen, E P, ***Hematite reconstruction of Late Triassic hydroclimate over the Colorado Plateau [J]****. Proceedings of the National Academy of Sciences, 2021, 118 (7).*

https://doi.org/10.1073/pnas.2004343118

摘要：近地表过程产生的赤铁矿是地球上最丰富的表层铁氧化物，对解决众多地质问题具有重要意义。虽然红层已被证明是记录古地磁信息的良好载体，但是在此类地质单元中赤铁矿的早期成岩成因却经常遭到质疑。我们通过对亚利桑那州钦迪组钻孔岩心 CPCP-PFNP13-1A 中 14.5-My-长红层序列进行分光光度法测定与分析，验证了赤铁矿染色矿物作为晚三叠纪环境及其准同源指示的可行性。赤铁矿染色矿物在红层中的含量可以追踪晚三叠纪季风的演变模式，并指示从~215Ma 开始的长期干旱趋势随后在~213Ma 出现了加剧的震荡性气候变化。这些季风性的变化归因于科罗拉多高原向北漂移，其作为劳伦古大陆的一部分，在二氧化碳波动的时期进入干旱的亚热带地区。我们的结果完善了晚三叠纪的季风记录，并表明在 Adamanian-Revueltian 生物过渡期边界降雨量发生了显著变化，从而可能导致了 216Ma 至 213Ma 之间明显的动植物事件。

ABSTRACT: Hematite is the most abundant surficial iron oxide on Earth resulting from near-surface processes that make it important for addressing numerous geologic problems. While red beds have proved to be excellent paleomagnetic recorders, the early diagenetic origin of hematite in these units is often questioned. Here, we validate pigmentary hematite (“pigmentite”) as a proxy indicator for the Late Triassic environment and its penecontemporaneous origin by analyzing spectrophotometric measurements of a 14.5-My–long red bed sequence in scientific drill core CPCP-PFNP13-1A of the Chinle Formation, Arizona. Pigmentite concentrations in the red beds track the evolving pattern of the Late Triassic monsoon and indicate a long-term rise in aridity beginning at ~215 Ma followed by increased oscillatory climate change at ~213 Ma. These monsoonal changes are attributed to the northward drift of the Colorado Plateau as part of Laurentia into the arid subtropics during a time of fluctuating CO_2. Our results refine the record of the Late Triassic monsoon and indicate significant

changes in rainfall proximal to the Adamanian–Revueltian biotic transition that thus may have contributed to apparent faunal and floral events at 216 to 213 Ma.

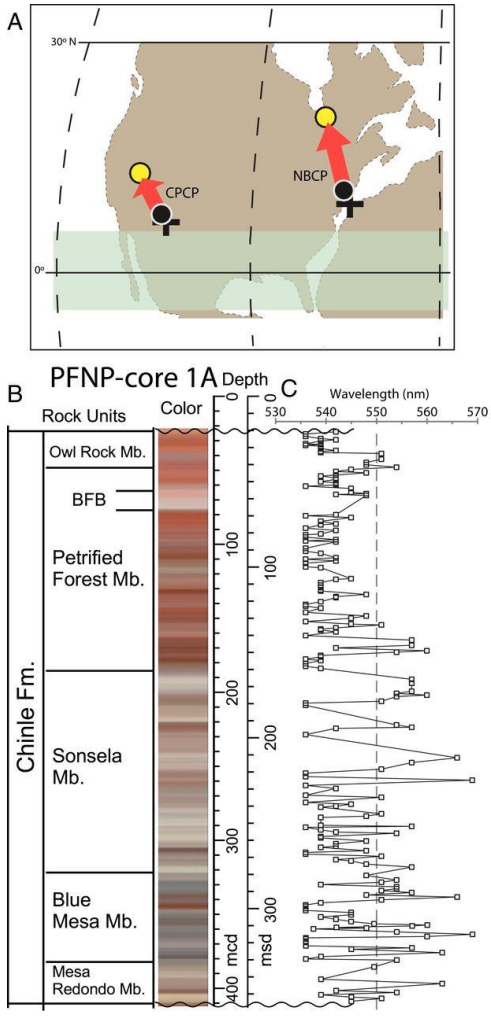

Figure 1. (A) Pangaean geography according to a 220-Ma mean composite paleopole (Kent et al., 2017) with the Chinle Formation (CPCP, Colorado Plateau Coring Project) and the Newark Basin (NBCP, Newark Basin Coring Project) indicated by filled circles connected by arrows to their relative positions at 200 Ma by open circles (Olsen et al., 2018). (B) Lithostratigraphic unit names, predominant colors, and thickness of the Chinle Formation in PFNP-core 1A (Kent et al., 2018; Kent et al., 2019; Olsen et al., 2018). (C) DRS results showing changes of the position of the characteristic absorption band for hematite. Note the very good agreement between the red (purple) colors of the core and wavelengths <550 nm (>550 nm).

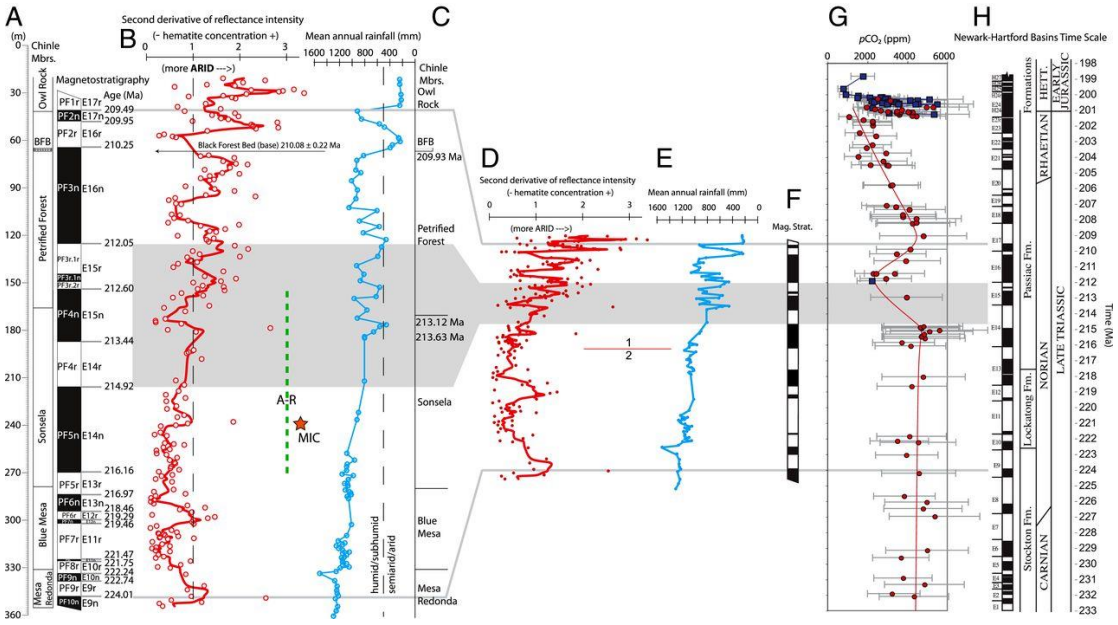

Figure 2. (A) Magneto-chronostratigraphy of the Chinle Formation in PFNP - core 1A (Kent et al., 2018; Kent et al., 2019; Olsen et al., 2018). BFB is the stratigraphic position of the Black Forest Bed dated within the core (Kent et al., 2018). (B) Second derivative values at ~535 to 570 nm of the intensity of hematite reflectance measured using DRS (this study). The thick red line is a six-point moving average of the (red circles) measured values. Hematite concentrations increase (more arid) toward the right. The green dashed line is the interval correlative to the Adamanian–Revueltian (A–R) biotic change (Kent et al., 2019; Parker et al., 2010). The orange star is the date of the Manicouagan impact crater (MIC) (Jaret et al., 2018; Ramezani et al., 2005). (C) Outcrop data of variations in mean annual rainfall (millimeters) from the CIA–K transfer function, with radioisotopic zircon dates for the BFB and volcaniclastic horizons in the upper Sonsela Member (Nordt et al., 2015; Atchley et al., 2014). (D) Hematite data stretched to time using the two accumulation rate intervals of ref. (Kent et al., 2019), with 1 being ~30 m/My and 2 being ~10 m/My. (E) Mean annual rainfall stretched to time as in D. (F) Chile magnetostratigraphy stretched to time as in D. (G) Late Triassic and Early Jurassic atmospheric pCO_2 (Schaller et al., 2014). The ± range bracketing the pCO_2 estimates is approximated using Monte Carlo simulation with the red trend line placed by the eye (Schaller et al., 2014). (H) Newark–Hartford astrochronostratigraphic polarity time scale (APTS) (Olsen et al., 1996; Kent et al., 2017). The gray shading indicates the magnetostratigraphic interval (chrons E14 and E15) that constrains the drawdown of pCO_2 at ~215 to 212 Ma. The gray lines indicate the interval of the Chinle magnetostratigraphy correlative to the Newark–Hartford APTS.

5. 蒸发岩风化与沉积是调控长时间尺度气候的控制因素

翻译人：仲义 zhongy@sustech.edu.cn

Graham, Shields A, Benjamin J W M, ***Evaporite weathering and deposition as a long-term climate forcing mechanism*** *[J] Geology, 2020, 49(3):299-303.*

https://doi.org/10.1130/G48146.1

摘要：尽管大家普遍认为，长期以来地球表面温度是硅酸盐风化作用和气候对二氧化碳的相互依赖作用所调节的，但一些气候事件的根本原因仍未得到解决。本文首次表明，蒸发岩风化与沉积的不平衡可以通过碳酸盐沉积过程影响气候。硫酸钙风化向海洋提供 Ca^{2+}离子，而不伴有碳酸盐碱度的变化，因此，碳酸盐沉淀的增加会加强二氧化碳向大气转移的温室强迫作用。相反，硫酸钙沉积减弱了温室效应，而蒸发岩的高沉积速率可能会超越硅酸盐风化的反馈作用，导致行星温度下降好几度。作为长期碳循环变化的驱动因素，非稳态蒸发岩动力学和相关反馈作用一直被忽视。在这里，本文通过展示中新世中晚期一系列大规模的沉积事件如何导致全球变冷来说明蒸发岩沉积的重要性。

ABSTRACT: Although it is widely accepted that Earth's long-term surface temperature is regulated by the mutual dependence of silicate weathering and climate on CO_2, the root causes of some climatic events remain unresolved. We show here for the first time that imbalances between evaporite weathering and deposition can affect climate through the process of carbonate sedimentation. Calcium sulfate weathering supplies Ca^{2+} ions to the ocean unaccompanied by carbonate alkalinity, so that increased carbonate precipitation strengthens greenhouse forcing through transfer of CO_2 to the atmosphere. Conversely, calcium sulfate deposition weakens greenhouse forcing, while the high depositional rates of evaporite giants may overwhelm the silicate weathering feedback, causing several degrees of planetary cooling. Non-steady state evaporite dynamics and related feedbacks have hitherto been overlooked as drivers of long-term carbon cycle change. Here, we illustrate the importance of evaporite deposition, in particular, by showing how a series of massive depositional events contributed to global cooling during the mid–late Miocene.

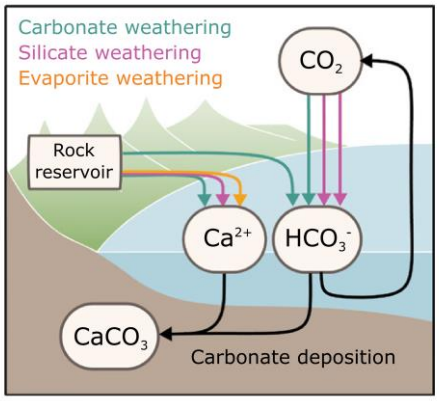

Figure 1. Delivery and removal of marine calcium and carbonate alkalinity. Three key weathering types are shown in different colors, where multiple arrows represent molar stoichiometry. Carbonate weathering (blue) transfers calcium and carbonate alkalinity from the continental rock reservoir, and CO_2 from the atmosphere, into the ocean. Carbonate deposition (black) reverses this process, removing alkalinity and calcium and releasing CO_2. Silicate weathering (purple) transfers calcium from the rock reservoir to the ocean, and it transfers two moles of carbon from the atmosphere to the ocean. Evaporite weathering (yellow) transfers only calcium to the ocean. Note that this is a simplification; see the model derivation in the Supplemental Material (see footnote 1) for all fluxes and processes.

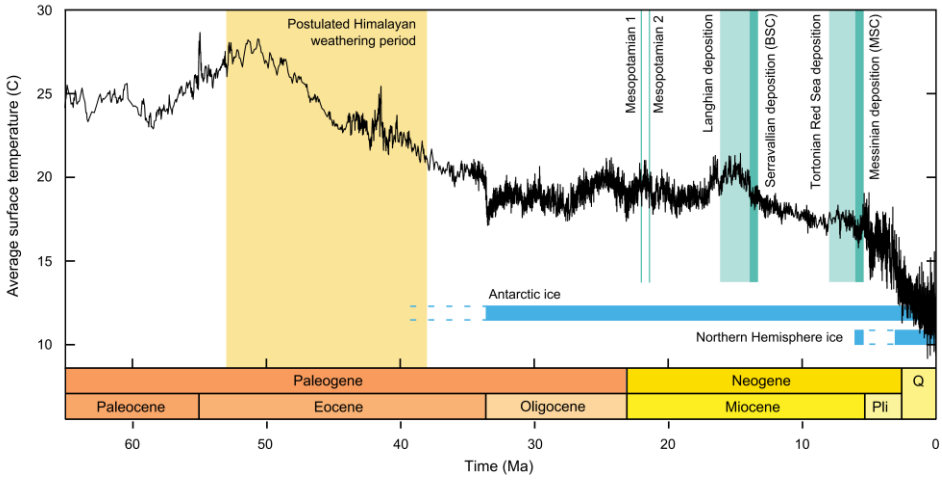

Figure 2. Cenozoic global average temperature versus evaporite events. Temperature record is from Hansen et al. (2013). The postulated period of evaporite weathering is shown as yellow, and known deposition events are shown as vertical teal bars. Horizontal blue bars show the existence of ice caps in the Northern and Southern Hemispheres. Pli—Pliocene; Q—Quaternary; BSC—Badenian salinity crisis; MSC—Messinian salinity crisis.

6. 东特提斯最东端中生代地壳生长:来自印度尼西亚苏门答腊花岗岩的 Hf 同位素证据

翻译人：周洋 zhouy3@sustech.edu.cn

Li S, Chung S, Lai Y M, et al. ***Mesozoic juvenile crustal formation in the easternmost Tethys: Zircon Hf isotopic evidence from Sumatran granitoids, Indonesia*** *[J]. Geology, 2020, 48:1002–1005.*

https://doi.org/10.1130/G47304.1

摘要：在印度板块与亚洲板块碰撞之前，东特提斯最东端岛弧演化和地壳的形成一直很难限制。在这里，我们首次报道了印度尼西亚苏门答腊中生代花岗岩锆石的 U-Pb 年龄和 Hf 同位素数据。我们发现存在 214-201 Ma，148-143 Ma 和 102-84 Ma 三期岩浆事件。晚三叠世花岗岩的锆石 ε Hf（t）值从-13.1 至+17.7，揭示了苏门答腊岛弧系统重组特征。随后，所有侏罗纪至晚白垩世花岗岩都具有正的锆石 ε Hf（t）值（+17.7 至+10.2），这与东特提斯最东端岩石圈向苏门答腊之下俯冲形成的新的岩浆弧具有一致性。苏门答腊花岗岩这种锆石 ε Hf（t）值与南亚的冈底斯弧的锆石 ε Hf（t）值很一致，都是以高正值为特征，与美洲和 Zealandia 广泛存在的同时代科迪勒拉弧（+13.7—-14.7）完全不一致，这不仅对东特提斯的构造岩浆演化提供了新见解，而且还为全球地壳生长提供了重要信息。

ABSTRACT: Prior to the collision of India with Asia, the evolution of island arcs and resultant crustal formation in the now-disrupted easternmost Tethys are poorly constrained. Here, we report for the frst time zircon U-Pb and Hf isotopic data from Mesozoic granitoids in Sumatra, Indonesia. Our analyses identifed three magmatic episodes at 214–201 Ma, 148–143 Ma, and 102–84 Ma, respectively, with a drastic change in magmatic zircon εHf(t) values from −13.1 to +17.7 in the Late Triassic granitoids, which reveals a fundamental restructuring of the arc system in Sumatra. Subsequently, all Jurassic to Late Cretaceous granitoids have exclusively positive zircon εHf(t) values (+17.7 to +10.2), consistent with juvenile arc development owing to subduction of the easternmost Tethyan lithosphere beneath Sumatra. Such highly positive zircon εHf(t) values of the Sumatran granitoids, in general accordance with those of the Gangdese arc system in South Asia,

are markedly higher than those (+13.7 to −14.7) of broadly contemporaneous Cordilleran arcs in Americas and Zealandia. Our findings from the easternmost Tethys provide new insights into not only the tectono-magmatic evolution of eastern Tethys, but also its crucial role in global juvenile crustal growth.

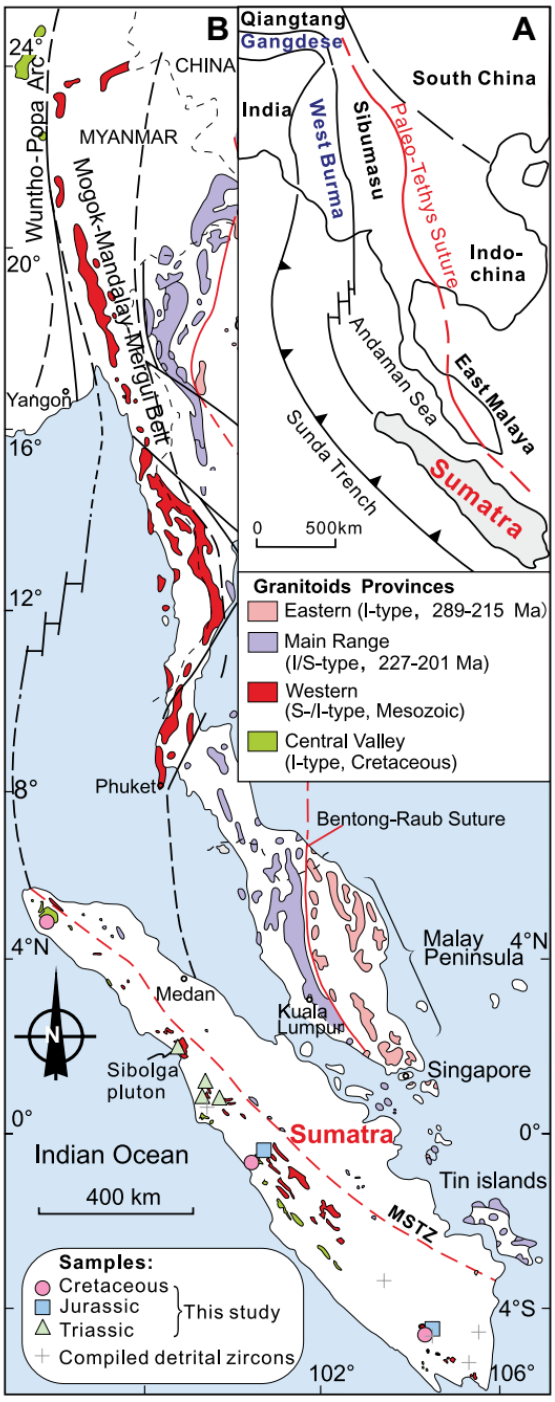

Figure 1. (A) Simplified tectonic map of Southeast Asia and adjacent regions, with major sutures and faults. (B) Simplified granite outcrop map of Southeast Asia, showing four granitoids provinces (after Gardiner et al., 2018). Compiled detrital zircon data are from Zhang et al. (2019). MSTZ—Medial

Sumatra tectonic zone. For details of Sumatran granitoids, see Figure S1 (text footnote 1).

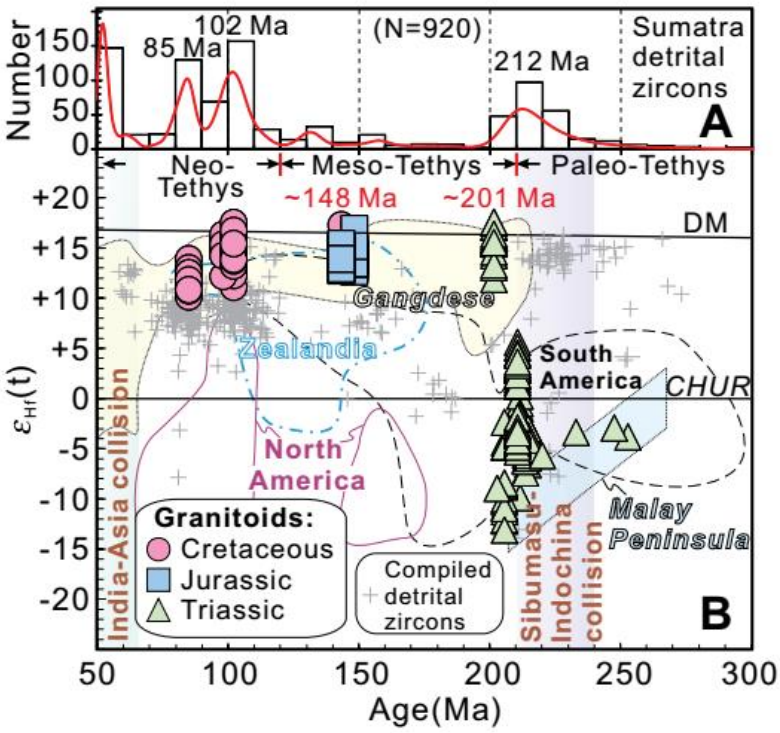

Figure 2. (A) Plot of detrital zircon age spectra for Sumatra. (B) Plot of zircon ages (Ma) vs. zircon εHf(t) values of Sumatran granitoids. Also plotted for comparison: Sumatra detrital zircons (gray cross symbols) and Gangdese arc (light-yellow area) from Zhang et al. (2019) and Malay Peninsula S-type granitoids (light blue area) from Liu et al. (2020). Lined areas denote Mesozoic Cordilleran arcs in North America (Chapman et al., 2018), South America (Mišković and Schaltegger, 2009; Cochrane et al., 2014; Bustamante et al., 2016), and Zealandia (Bolhar et al., 2008; Scott et al., 2009; Milan et al., 2017), respectively. DM—depleted mantle; CHUR—chondritic uniform reservoir.

7. 航磁资料对 Knipovich 洋脊扩张演化的新解释

翻译人：曹伟 11930854@QQ.com

Dumais M , Gernigon L , Olesen O , et al. ***New interpretation of the spreading evolution of the Knipovich Ridge derived from aeromagnetic data****[J]. Geophysical Journal International,2021, 224(2):1423-1429.*

https://doi.org/10.1093/gji/ggaa508

摘要：最近的航磁调查揭示了 Knipovich 洋脊扩张演化和 Fram 海峡打开的过程。作为位于斯瓦尔巴-巴伦支海和格陵兰岛东北裂谷边缘之间倾斜系统中的一个超低速扩张脊，Knipovich 洋脊扩张的动力学一直存在争议。它与 Mohns 洋脊呈 90°弯曲，这在板块构造中是罕见的，同时影响了 Fram 海峡的演化，并推动了这种独特结构的地壳形变研究。我们识别了现今 Knipovich 洋脊两侧的磁异常等时线。这些磁性观测很大程度上减少了海洋区域的映射范围，并对目前共轭裂谷边缘的观点提出质疑。我们的分析表明，在 Fram 海峡进行大规模扩张重组之前（大约在磁极 C6，即大约 20 Ma），扩张体系停止扩张。

ABSTRACT: Insights into the spreading evolution of the Knipovich Ridge and development of the Fram Strait are revealed from a recent aeromagnetic survey. As an ultraslow spreading ridge in an oblique system located between the Svalbard–Barents Sea and the Northeast Greenland rifted margins, the dynamics of the Knipovich Ridge opening has long been debated. Its 90◦ bend with the Mohns Ridge, rare in plate tectonics, affects the evolution of the Fram Strait and motivates the study of crustal deformation with this distinctive configuration. We identified magnetic isochrons on either side of the present-day Knipovich Ridge. These magnetic observations considerably reduce the mapped extent of the oceanic domain and question the present understanding of the conjugate rifted margins. Our analysis reveals a failed spreading system before a major spreading reorganization of the Fram Strait gateway around magnetic Chron C6 (circa 20 Ma).

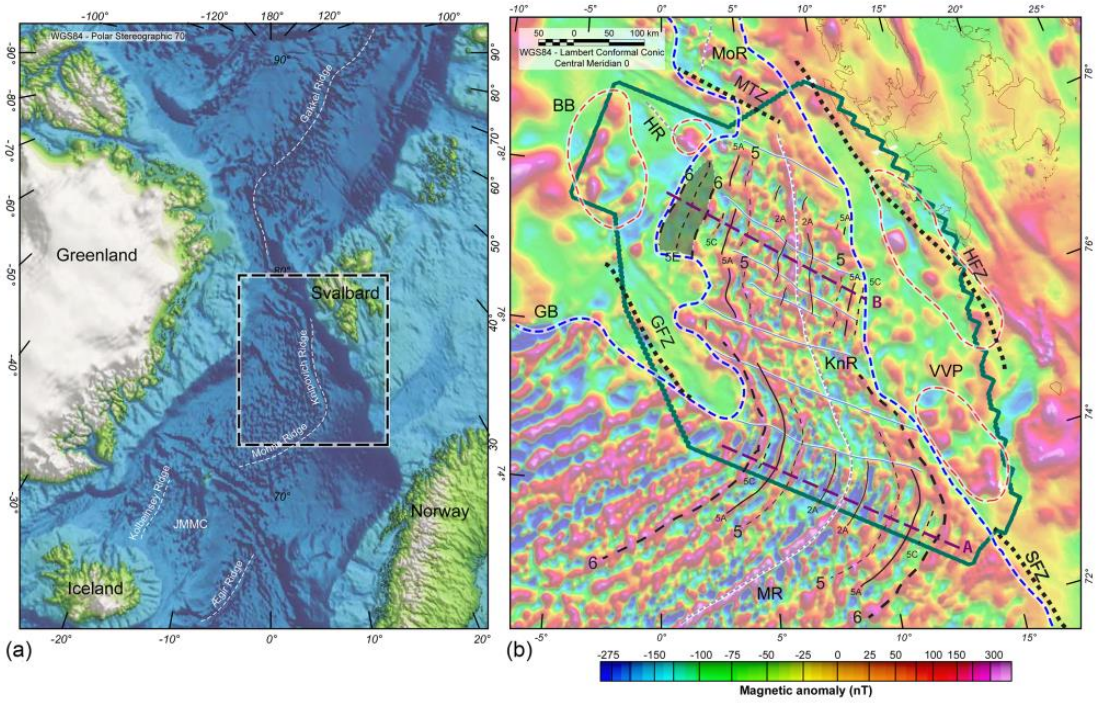

Figure 1. Survey area and aeromagnetic data. (a) Location of the Knipovich Ridge with respect to the North Atlantic realms with SRTM topographic data. (b) The new aeromagnetic data revealed the timing of the breakup (C6) and magmatic events on the eastern side of the ridge. Profiles A and B are in purple. MoR: Molloy Ridge; MTZ: Molloy Transform Zone; HR: Hovgaard Ridge; BB: Boreas Basin; HFZ: Hornsund Fracture Zone; KnR: Knipovich Ridge; GFZ: Greenland Fracture Zone; GB: Greenland Basin; JMMC: Jan Mayen Microplate Complex; VVP: Vestbakken Volcanic Province; MR: Mohns Ridge; SFZ: Senja Fracture Zone. New oceanic fracture zones are displayed with grey lines, new COB demarcation is in dashed blue line and volcanic areas are delimited by the dashed red lines. The abandoned ridge is highlighted in grey shading.

8. 珠江口盆地白云凹陷后裂陷期海底火山杂岩与断裂活动：对南海北部破裂层序的新认识

翻译人：刘伟 inewway@163.com

Zhou W, Zhuo H T, Wang Y M, et al. ***Post-rift submarine volcanic complexes and fault activities in the Baiyun Sag, Pearl River Mouth Basin: New insights into the breakup sequence of the northern South China Sea****[J]. Marine Geology, 2020, 430.*

https://doi.org/10.1016/j.margeo.2020.106338

摘要：后裂陷期火山作用和断层活动对了解裂陷型大陆边缘构造-沉积演化及相关油气圈闭具有重要意义。本研究在南海北部大陆边缘发现了一系列与后裂陷期断裂有关的火山活动。然而，其与大陆破裂的关系仍然不太明确。利用新的二维、三维地震、钻孔、测年和生物地层学资料，研究了珠江口盆地白云凹陷后裂陷期火山活动和断裂活动特征。新发现的断层相关火山杂岩包括 13 个海底火山丘和相关熔岩流，以及主要由玄武岩和凝灰岩组成的火成岩床。地震地层学分析结合岩心 K-Ar 测年证实，白云凹陷后裂陷期火山作用随南海破裂而达到高潮，主要有三幕：（1）渐新世/中新世界线附近的第一幕（23.3Ma）；（2）早中新世中期的第二幕（17.6Ma）；（3）新发现的在早中新世（17.1 Ma）的第三幕。此外，还解释了 53 条同沉积断层，其特征是由一系列北西西向的正断层组成，并被北东东向的走滑断层分开。有证据表明，这 53 条断层在约 32-17.1 Ma 的时间内存在很长时间，是岩浆向上运移的重要通道。三次火山作用和构造断裂活动与南海北部陆缘的渐进式大陆破裂有关，它们代表了岩石圈破裂后在后裂陷沉降早期的构造特征，并延伸至白云凹陷的破裂层序（32－17.1 Ma）的顶部。此外，本研究还证明，南海边缘的穿时大陆破裂可导致沉积结构的相应变化，以及以“砂岩-碳酸盐岩-页岩”海侵旋回沉积为特征的破裂层序。白云凹陷的沉积学变化和相关构造特征表明，南海北部边缘的破裂层序（早渐新世-早中新世）形成时，构造环境异常活跃。

ABSTRACT: Post-rift volcanisms and fault activities are significant for understanding the tectonic-sedimentary evolution of rifted continental margins and associated hydrocarbon entrapments. In this study, a series of post-rift fault-associated volcanic activities have been found

in the northern continental margin of the South China Sea (SCS). However, their episodes and relationships with the progressive continental breakup are still doubtful. Here, new 2D/3D seismic, borehole, dating, and biostratigraphic data are used to investigate the characteristics of the post-rift volcanism and fault activities in the Baiyun Sag (BYS), Pearl River Mouth Basin. The newly-found fault-associated volcanic complexes include thirteen submarine volcanic mounds and associated lava flows, together with igneous sills that are mainly composed of basalts and tuffs. Seismic stratigraphic analysis combined with K-Ar dating from cores confirms that post-rift volcanism in the BYS climaxed along with the breakup of the SCS mainly in three episodes: (1) the first episode near Oligocene/Miocene boundary (23.3 Ma); (2) the second at the middle Early Miocene (17.6 Ma); and (3) the new-found third episode at the late Early Miocene (17.1 Ma). Also, fifty-three syn-sedimentary faults are interpreted, which are characterized by a WNW trending normal fault group separated by an ENE trending transcurrent fault group. And there is evidence that these fifty-three faults were long-lived from ca. 32–17.1 Ma and served as important conduits for the upward migration of the magma. The three episodes of volcanism and tectonic fault activities are related to the progressive continental breakup in the northern SCS margin, and they represent the tectonic signature of the early stage of the post-rift subsidence after the lithospheric breakup which extends to the top of a hypothetical breakup sequence (32–17.1 Ma) in the BYS. Furthermore, this study proves that the diachronous continental breakup in the SCS margin can result in corresponding changes in depositional architectures, along with a breakup sequence characterized by the deposition of a ‘sandstone-carbonate-shale’ regressive-transgressive cycle. The sedimentological changes and associated tectonic features recorded in the Baiyun Sag suggest an exceptionally active tectonic setting in the time of the formation of the breakup sequence (Early Oligocene-Early Miocene) along the northern SCS margin.

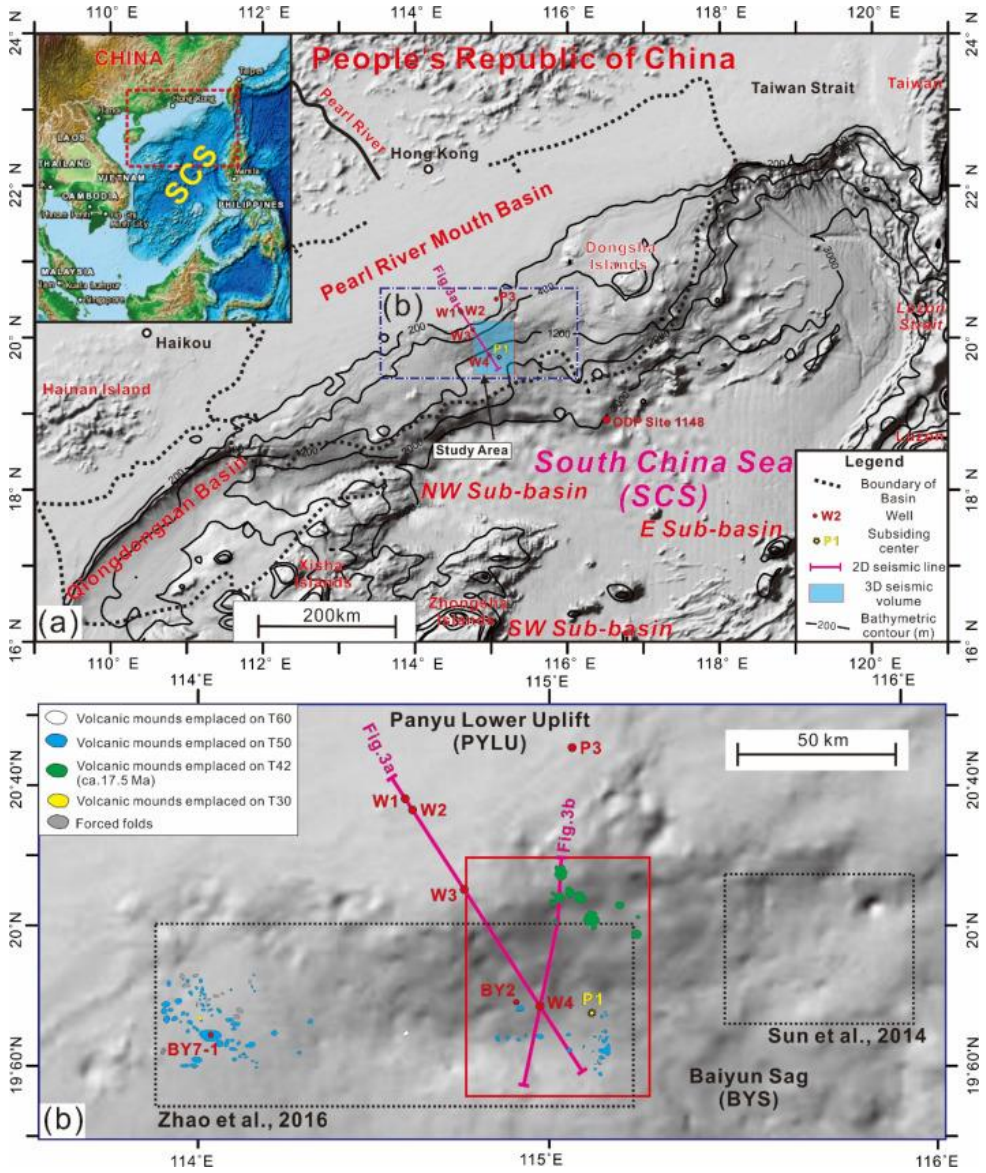

Figure 1. (a) Regional locations of the study area and the Pearl River Mouth Basin (PRMB). The study area is located in the proximal of the continent-ocean transition zone of the northern South China Sea (SCS) margin (Baiyun Sag of PRMB). The magenta line and the red square filled with blue outline the 2D multichannel seismic line and 3D seismic dataset, respectively. The SCS basin is divided into the E Sub-basin, the NW Sub-basin and the SW Sub-basin; (b) The enlargement of the study area illustrating the distribution of volcanic mounds in the study area. The locations of figures are labeled. The volcanic mounds emplaced on T60, T50, T30 and the forced folds are referenced from Zhao et al. (2016). The locations of seven wells (W-W4, BY2, BY7–1, P3) and the subsiding center of the Baiyun Sag (P1) are labeled. Among them, wells BY7–1 and BY2 are referenced from Zhao et al. (2016), Well P3 and Point P1 are from Xie et al. (2014).

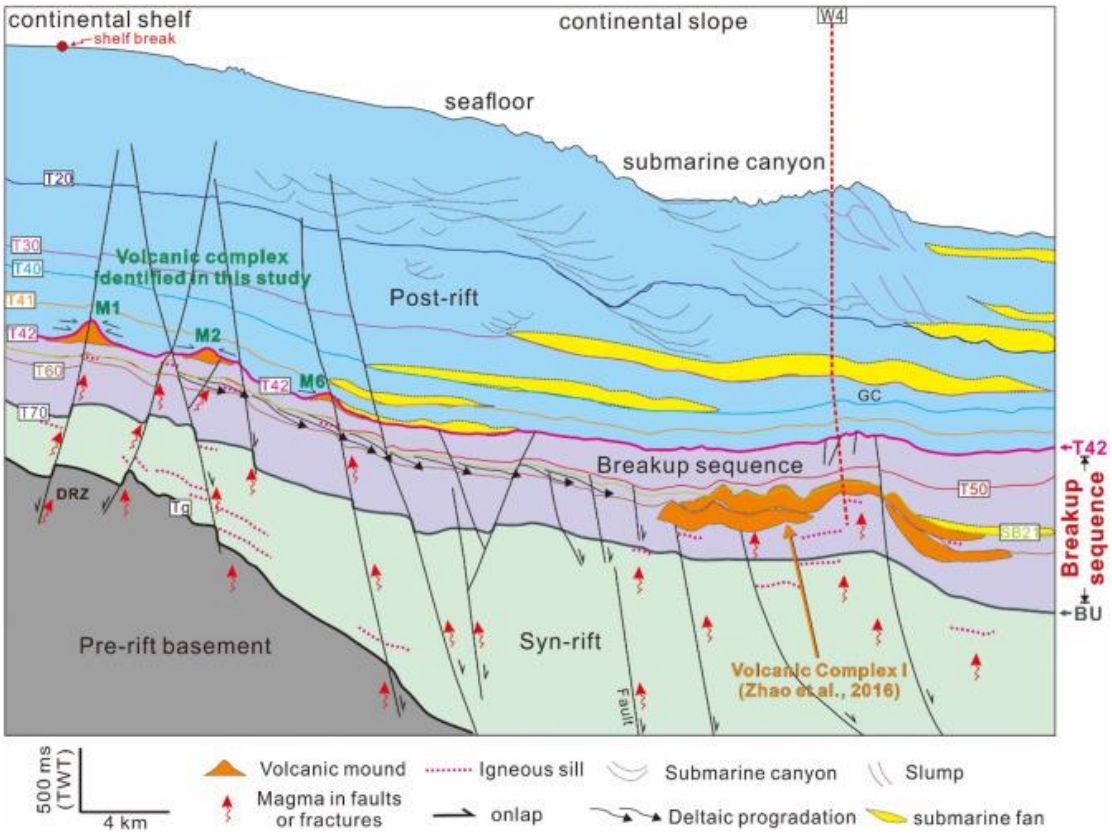

Figure 2. Schematic illustration showing the formation of volcanic complex (three episodes) in relation to the Early Oligocene-Early Miocene breakup sequence of the Baiyun Sag. Seismic reflector T70 is the breakup unconformity (BU) of the northern SCS margin. Seismic reflector T42 is the top boundary of this breakup sequence. DRZ: zones of dim reflections.

9. 季风降雨氧同位素组成的记录者：中国黄土微松藻

翻译人：杨会会 11849590@mail.sustech.edu.cn

Zhang Z K, Li G J, Yan H, et al. ***Microcodium in Chinese loess as a recorder for the oxygen isotopic composition of monsoonal rainwater****[J].Quaternary International, 2018, 464:364-369.*
https://doi.org/10.1016/j.quaint.2017.10.050

摘要： 来自中国黄土和石笋的亚洲夏季风记录展示出了不同的特征。应用于这两种记录的差异显著的指标可能造就了这种不一致。石笋和黄土记录在同一降水氧同位素指标体系下的直接对比可能有助于解决这一困惑。本文我们揭示了黄土沉积中钙化微松藻可能记录了夏季降水的氧同位素组成。一条过去 140 ka 微松藻氧同位素记录，展现出了与石笋氧同位素记录全面变化相类似的变化幅度，但是在末次间冰期时期微松藻记录的岁差变率却要弱得多。然而，微松藻氧同位素记录和被广泛用于指示夏季风的黄土磁化率指标在冰期-间冰期模式上的清晰变化表现上却更为一致。这一相似性可能源于间冰期古土壤层的低沉积速率，同时优先记录了弱的亚洲夏季风岁差信号。也可能伴随着北方受到更多冰量影响，华北和华南在亚洲夏季风轨道尺度变率上有一些内在的差异。这样以来，一条更长尺度在更高沉积速率序列下的微松藻氧同位素记录和一条可靠的夏季降水记录可能就有助于解决这些不同的可能性疑惑。

ABSTRACT: Records of Asia Summer Monsoon (ASM) from the Chinese loess and the speleothem display distinct features. The very different proxies that were applied to the two archives may be responsible for this discrepancy. A direct comparison between the speleothem and the loess records under the same proxy system of rainwater $\delta^{18}O$ may help to resolve this puzzle. Here we show that the calcified microcodium in the loess deposits may record the oxygen isotopic composition of the summer rainwater. A microcodium based $\delta^{18}O$ record covering the past 140 kyrs was generated, which shows similar magnitude of the overall variation to that of the speleothem records. However, much weaker precession variability was registered in the microcodium record

during the last interglacial period. Instead, the microcodium $\delta^{18}O$ record is more consistent with the widely used summer monsoon proxy of magnetic susceptibility in the loess deposits with clear glacial-interglacial pattern. This similarity may originate from the low sedimentation rate of the interglacial paleosol layer that preferentially record the peak ASM signals on the precession band. It is also possible that the orbital variability of ASM between the North China and South China is inherently different with more ice-volume related influence in the north. A longer microcodium $\delta^{18}O$ record in sequences of higher sedimentation rate and a reliable record of summer rainfall may help to resolve these possibilities.

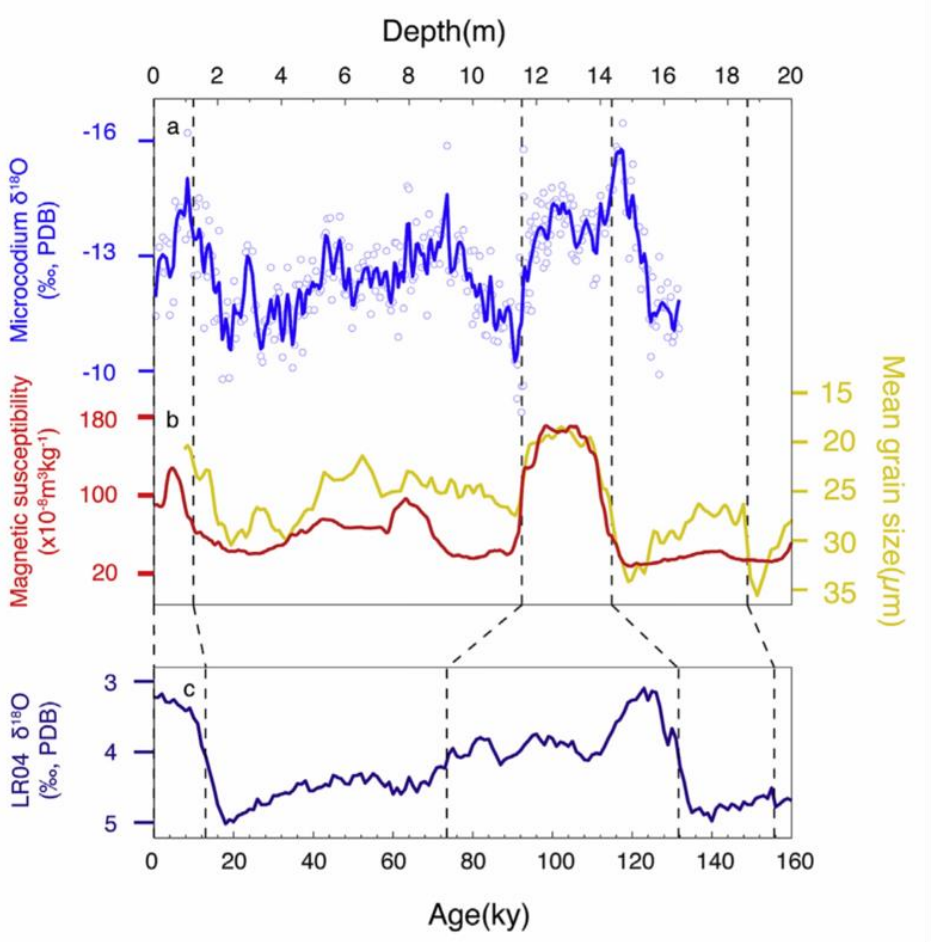

Figure 1. The microcodium $\delta^{18}O$ record in Xifeng section and age model. (a) Microcodium $\delta^{18}O$ record plotted on depth scale (smoothed by a 5-cm width Gaussian filter). (b) Mean grain size of quartz (yellow)(Sun et al., 2006) and MS (red) plotted on depth scale. (c) LR04 composite of benthic $\delta^{18}O$ (Laskar et al., 2004). Vertical dash lines show the tie points of the age model. (For interpretation of the references to color in this figure legend, the reader is referred to the web version of this article.)

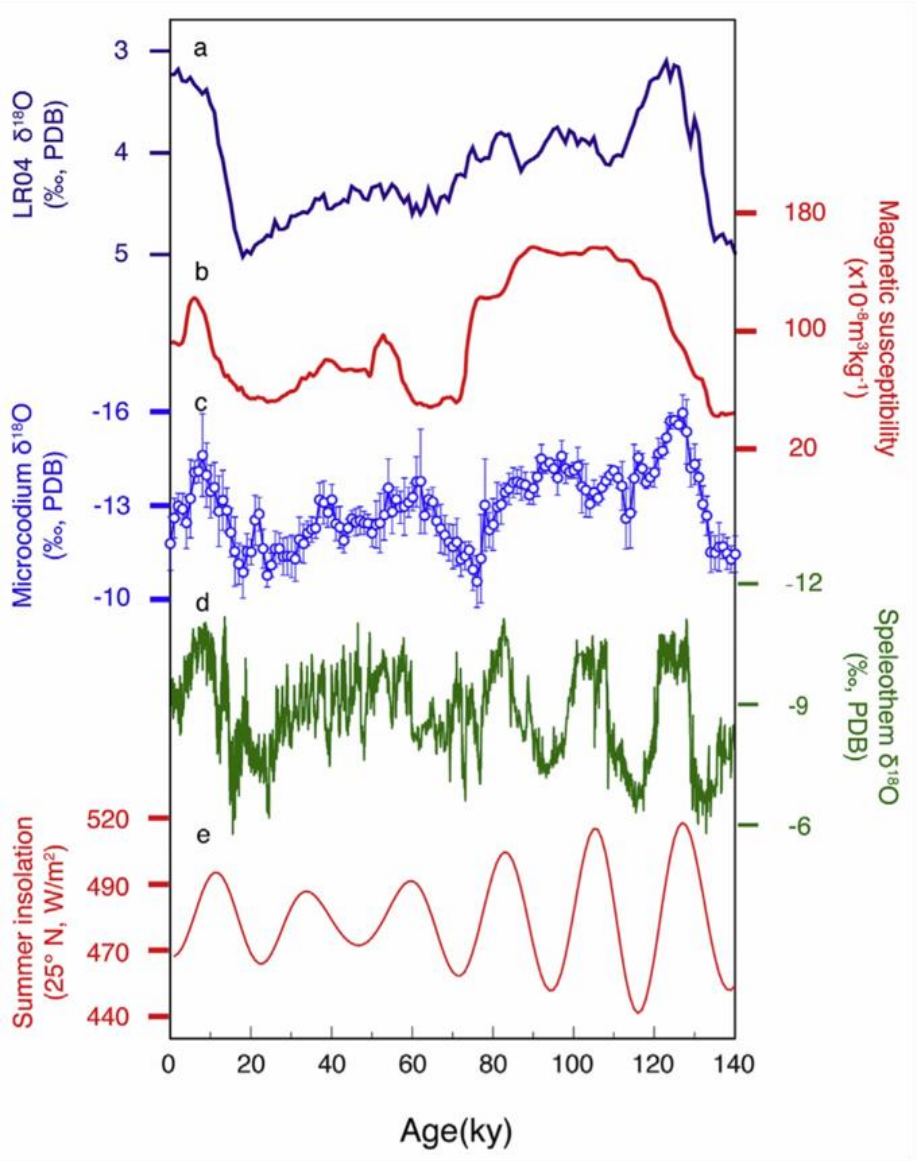

Figure 2. Comparing the microcodium $\delta^{18}O$ record with other time series. (a) LR04 composite of deep seawater $\delta^{18}O$ that reflects global ice volume (Lisiecki and Raymo, 2005). (b) The loess magnetic susceptibility. (c) The stacked microcodium $\delta^{18}O$ with error bar showing 2× standard error of the stacked mean (open cycles are smoothed record using a 0.5-ky Gaussian filter). (d) Speleothem $\delta^{18}O$ (Cheng et al., 2016). (e) The summer (June 21st) insolation at 25°N.

10. 东白令海晚第四纪海冰和沉积物氧化还原条件对北太平洋中深水通风和大西洋—太平洋跷跷板机制的影响

翻译人：张亚南 zhangyn3@mail.sustech.edu.cn

Henrieka D, Sindia M S, Simon T B, et al. ***Late quaternary sea-ice and sedimentary redox conditions in the eastern Bering Sea - Implications for ventilation of the mid-depth North Pacific and an Atlantic-Pacific seesaw mechanism*** *[J].Quaternary Science Reviews, 2020, 248, 106549.*

https://doi.org/10.1016/j.quascirev.2020.106549

摘要：在冰期—间冰期和千年尺度上，海冰对高纬区环流和生产力具有重要的作用，影响着区域和全球的生物地球化学循环。在现代的北太平洋，鄂霍茨克海海冰的生成，使得盐分析出，驱动了北太平洋中层水（NPIW）的形成，其通风深度在 300-1000m。晚第四纪冰期 NPIW 至少加深至 2000m，并在末次间冰期的冷阶段记录到了最强的通风。然而，NPIW 通风转变的起因还不清楚。数值模拟表明，北大西洋和北太平洋之间的大气遥相关，是对大西洋经向翻转流减缓或停止的反映。这导致了北太表层海水盐度的累积，从而引发深层通风。另一方面，北太平洋及其边缘海海冰的增加可能加强了盐分的析出，使得海水密度变大，从而产生更强的水体交换。文中，作者通过多指标探讨了东白令海 IODP 钻孔 U1343 孔 40ka 以来的海冰动态变化、沉积物氧化还原和底栖生态。结果表明，H1 早期海冰形成加强导致的盐分析出局部削弱了盐跃层，有助于了深部水体翻转的开始。此外，冰消期暖阶段海冰的后退可能导致了 U1343 孔初级生产力的增加和中层缺氧带的扩张，证实了海冰在北太平洋冰消期碳循环中的重要性。

ABSTRACT: On glacial-interglacial and millennial timescales, sea ice is an important player in the circulation and primary productivity of high latitude oceans, affecting regional and global biogeochemical cycling. In the modern North Pacific, brine rejection during sea-ice freezing in the Sea of Okhotsk drives the formation of North Pacific Intermediate Water (NPIW) that ventilates the North Pacific Ocean at 300 me1000 m water depth. Glacial intervals of the late Quaternary, however,

experienced a deepening of glacial NPIW to at least 2000 m, with the strongest ventilation observed during cold stadial conditions of the last deglaciation. However, the origin of the shifts in NPIW ventilation is poorly understood. Numerical simulations suggest an atmospheric teleconnection between the North Atlantic and the North Pacific, in response to a slowdown or shutdown of the Atlantic meridional overturning circulation. This leads to a build-up of salinity in the North Pacific surface ocean, triggering deep ventilation. Alternatively, increased sea-ice formation in the North Pacific and its marginal seas may have caused strengthened overturning in response to enhanced brine rejection.Here we use a multi-proxy approach to explore sea-ice dynamics, sedimentary redox chemistry, and benthic ecology at Integrated Ocean Drilling Program Site U1343 in the eastern Bering Sea across the last 40 ka. Our results suggest that brine rejection from enhanced sea-ice formation during early Heinrich Stadial 1 locally weakened the halocline, aiding in the initiation of deep overturning. Additionally, deglacial sea-ice retreat likely contributed to increased primary productivity and expansion of mid-depth hypoxia at Site U1343 during interstadial conditions, confirming a vital role of sea ice in the deglacial North Pacific carbon cycle.

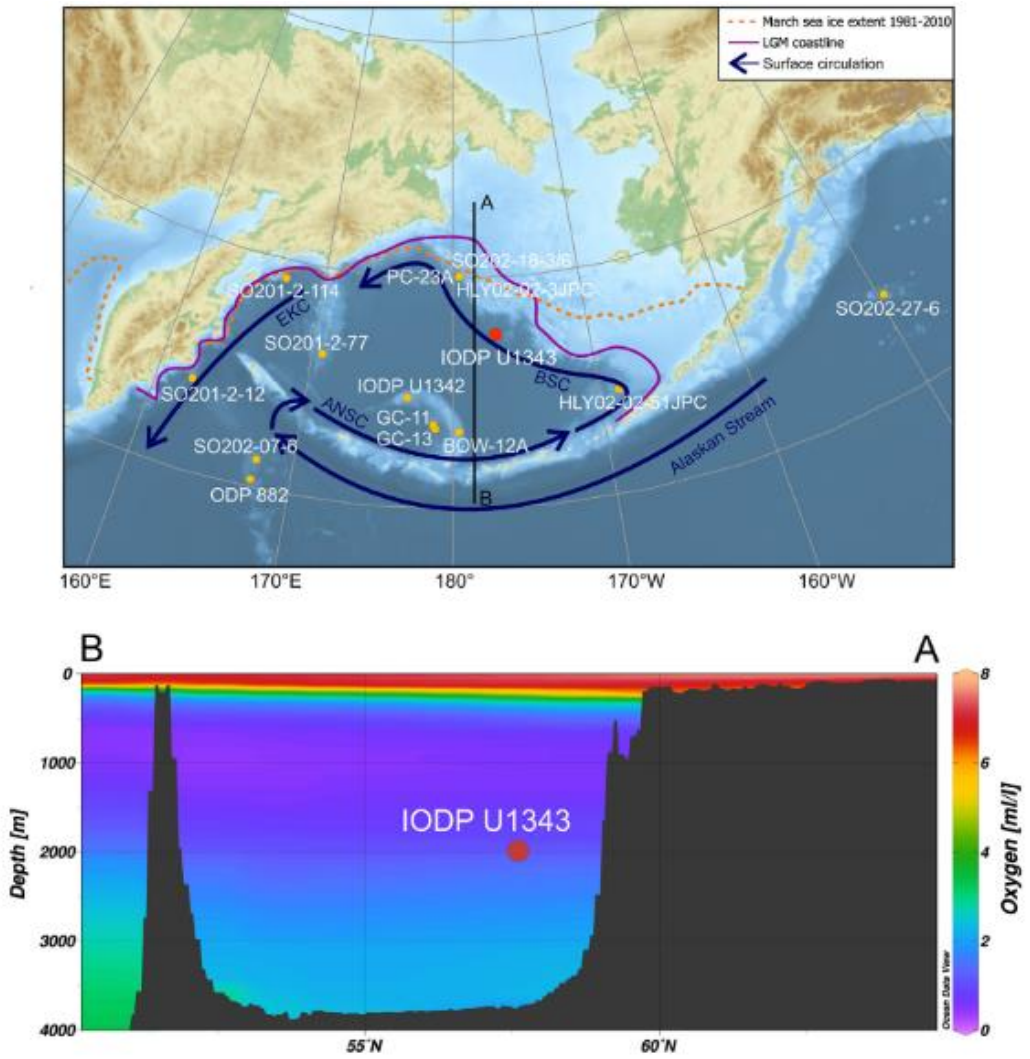

Figure 1. Map of the Bering Sea (top) and annual mean oxygen concentrations (Boyer et al., 2013) along a north (A) south (B) transect in the central Bering Sea (bottom) drawn with Ocean Data View (Schlitzer, 2016) (bathymetry from 'The GEBCO_2014 Grid, version 20,141,103'). IODP Site U1343 is indicated with a red dot, additional core locations discussed in the text are marked with yellow dots. The map shows the surface ocean circulation (dark blue), including the Alaskan Stream, the Aleutian North Slope Current (ANSC), the Bering Slope Current (BSC), and the East Kamchatka Current (EKC). The maximum winter sea-ice extent between 1981 and 2010 is indicated as an orange dashed line (Fetterer et al., 2017) and the last glacial maximum (LGM) coastline is shown in purple (The PALE Beringian Working Group, 1999).

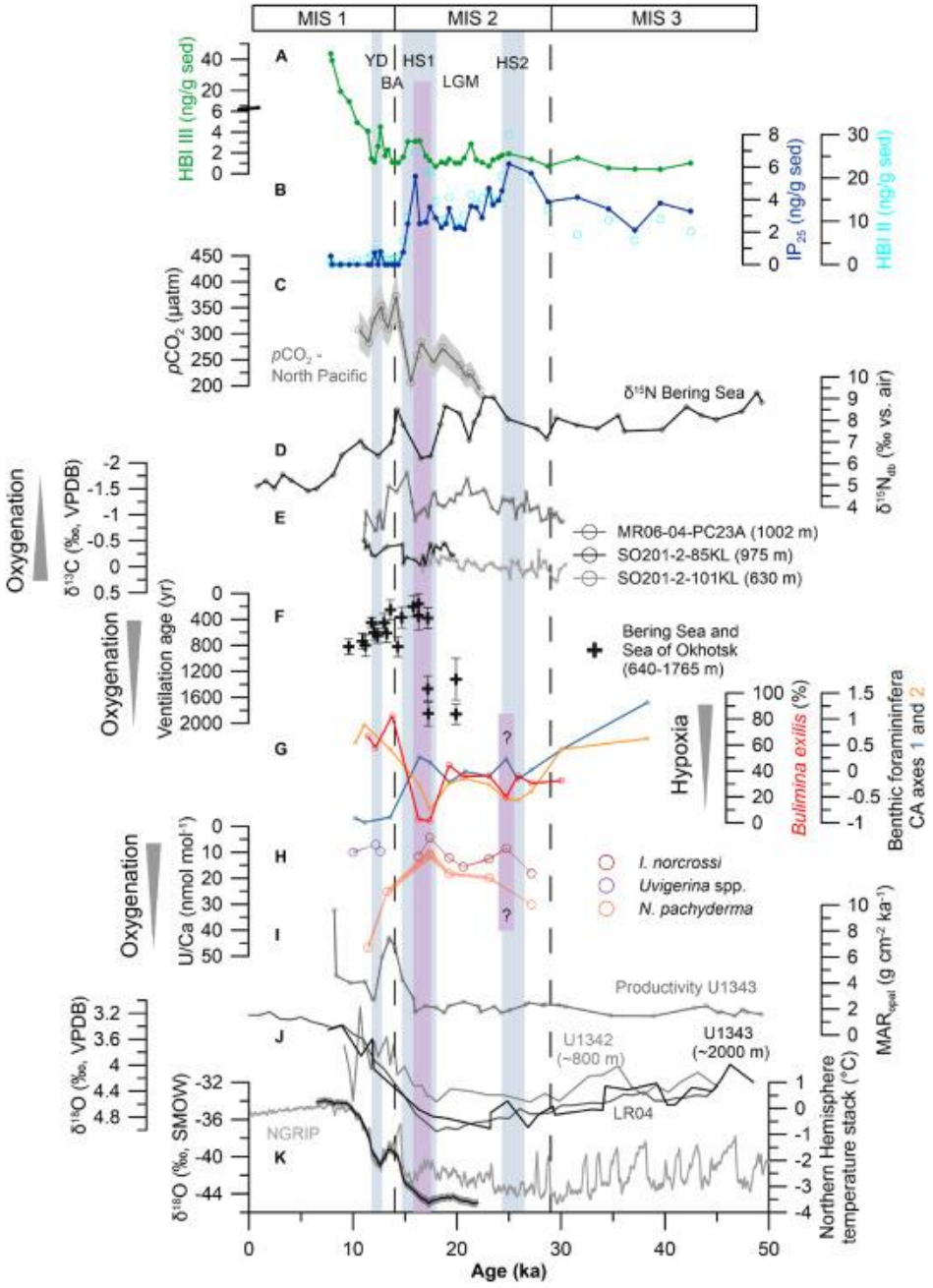

Figure 2. A compilation of ventilation and carbon cycle records discussed in this manuscript in combination with regional and global climate records. (A) HBI III (green) at Site U1343 (this study); (B) IP25 (dark blue) together with HBI II (light blue circles) (this study); (C) North Pacific pCO_2 at MD01-2416 (Gray et al., 2018); (D) Diatom-bound $\delta^{15}N$ at JPC17 (Brunelle et al., 2007); (E) Benthic foraminiferal $\delta^{13}C$ at MR06-04-PC23A (medium grey) (Rella et al., 2012), SO201-2-85 KL (dark grey), and SO201-2-101 KL (light grey) (Max et al., 2014); (F) Intermediate water ventilation ages in the Bering Sea and the Sea of Okhotsk (Max et al., 2014); (G) Scores of the benthic foraminiferal assemblage correspondence analysis axis 1 (blue) and 2 (yellow) and the relative abundance of the benthic

foraminifera Bulimina exilis (red) at Site U1343; (H) U/Ca of N. pachyderma (orange), I. norcrossi (red), and Uvigerina spp. (purple) at Site U1343; (I) MARopal at Site U1343 (Kim et al., 2014); (J) Benthic foraminiferal δ18O at IODP Site U1342 (light grey) (Knudson and Ravelo, 2015), Site U1343 (black) (Asahi et al., 2016), and the LR04 stack (grey) (Lisiecki and Raymo, 2005); (K) NGRIP δ18O on the GICC05 time scale (Rasmussen et al., 2006; Svensson et al., 2008; Vinther et al., 2006), and the Northern Hemisphere temperature stack including a 1σ error envelope (Shakun et al., 2012). The light blue shaded vertical bars indicate the YD, HS1, and HS2, the pink vertical bars indicate intervals with imrpoved ventilation at Site U1343.

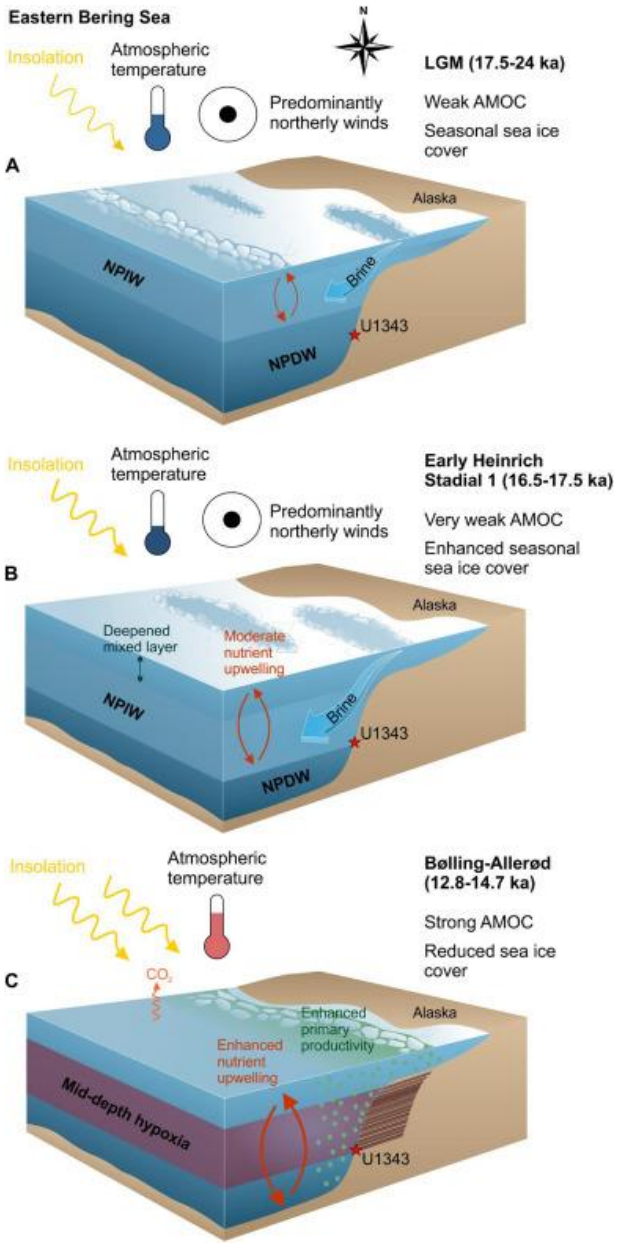

Figure 3. Simplified schematic of the deglacial sea-ice dynamics, intermediate water ventilation, and biogeochemical cycling in the eastern Bering Sea. The schematic was produced using features from the IAN symbol library (Courtesy of the Integration and Application Network, University of Maryland Center for Environmental Science (ian.umces.edu/symbols/)). (A) The LGM (17.5–24 ka) was characterized by a seasonal sea-cover, reduced upwelling of NPDW, and an expanded GNPIW resulting from enhanced brine rejection. GNPIW, however, did not reach to depth of 2000 m. (B) Early HS1 (16.5–17.5 ka) was characterized by an enhanced seasonal sea-ice cover, in response to atmospheric cooling. Increased sea-ice formation led to enhanced brine rejection and increased GNPIW formation and ventilation compared to the LGM, which in turn caused modest up-mixing of nutrients, as well as a deepening of the mixed layer resulting in light limitation of primary producers. (C) The BA (12.8–14.7 ka) is marked by a reduced sea-ice cover due to atmospheric warming, enhanced NPDW upwelling, increased primary productivity, and pronounced mid-depth hypoxia causing the preservation of laminations along the eastern Bering Sea slope.

11. 低对流层过程，控制全球平均降水率

翻译人：李海 12031330@mail.sustech.edu.cn

Hendrickson J M, Terai C R, Pritchard M S, et al. ***Lower Tropospheric Processes: A Control on The Global Mean Precipitation Rate****. Geophysical Research Letters,2021, 48, e2020GL091169.*
https://doi.org/10.1029/2020GL091169

摘要: 利用表面蒸发和能量收支的互补观点，在两个气候模型中探讨全球平均降水的差异。受近地表干燥空气的驱动，全球平均降水量较高的模型的海洋蒸发更强。在 925 hPa 时，在干燥的地表条件下温度和湿度同时增加，表明边界层混合更强。相关性表明，对流层较低的混合解释了模式间 18%-49%的降水差异。为了检验该假设，在单个模型实验中，通过调整控制低云量的相对湿度阈值，间接改变了混合程度。对流层低层混合的增加导致了全球平均降水的增多。从能量上讲，降水速率的增加与更强的地面长波辐射和更弱的感热通量有关。这些结果强调了如何更好地约束低对流层过程，以减少气候模型之间的降水差异。

ABSTRACT: The spread in global mean precipitation among climate models is explored in two ensembles using the complementary perspectives of surface evaporation and energy budgets. Models with higher global-mean precipitation have stronger oceanic evaporation, driven by drier near-surface air. The drier surface conditions occur alongside increases in near-surface temperature and moisture at 925 hPa, which point to stronger boundary layer mixing. Correlations suggest that the degree of lower tropospheric mixing explains 18% - 49% of the intermodel precipitation variance. To test this hypothesis, the degree of mixing is indirectly varied in a single-model experiment by adjusting the relative humidity threshold that controls low-cloud fraction. Indeed, increasing lower tropospheric mixing results in more global mean precipitation. Energetically, increased precipitation rates are associated with more downwelling longwave radiation to the surface and weaker sensible heat fluxes. These results highlight how lower-tropospheric processes must be better constrained to reduce the precipitation discrepancy among climate models.

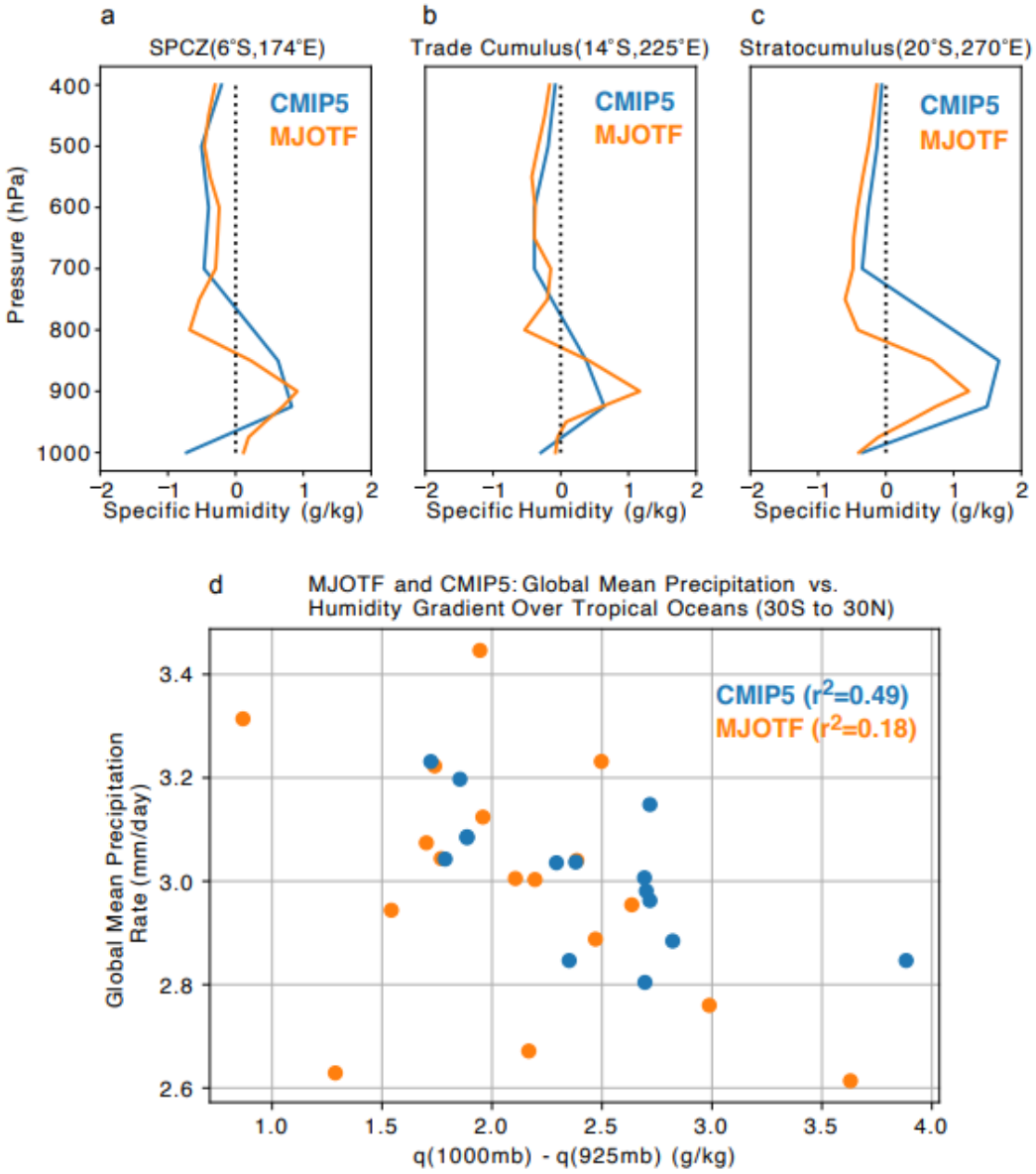

Figure.1 (a-c) Time averaged specific humidity anomalies at 3 locations from climate models participating in the MJO Task Force intercomparison (MJOTF - orange) and in the Atmospheric Model Intercomparison Project of CMIP5 (CMIP5 - blue). Anomalies represent differences between the 5 rainiest and 5 driest models in each ensemble. The geographic locations of these profiles noted in Fig. S3. (d) The specific humidity difference between 1000hPa and 925hPa, averaged over tropical oceans is plotted against the global mean precipitation rates. Each CMIP5 model is indicated by a blue dot while the MJOTF models are displayed in orange.

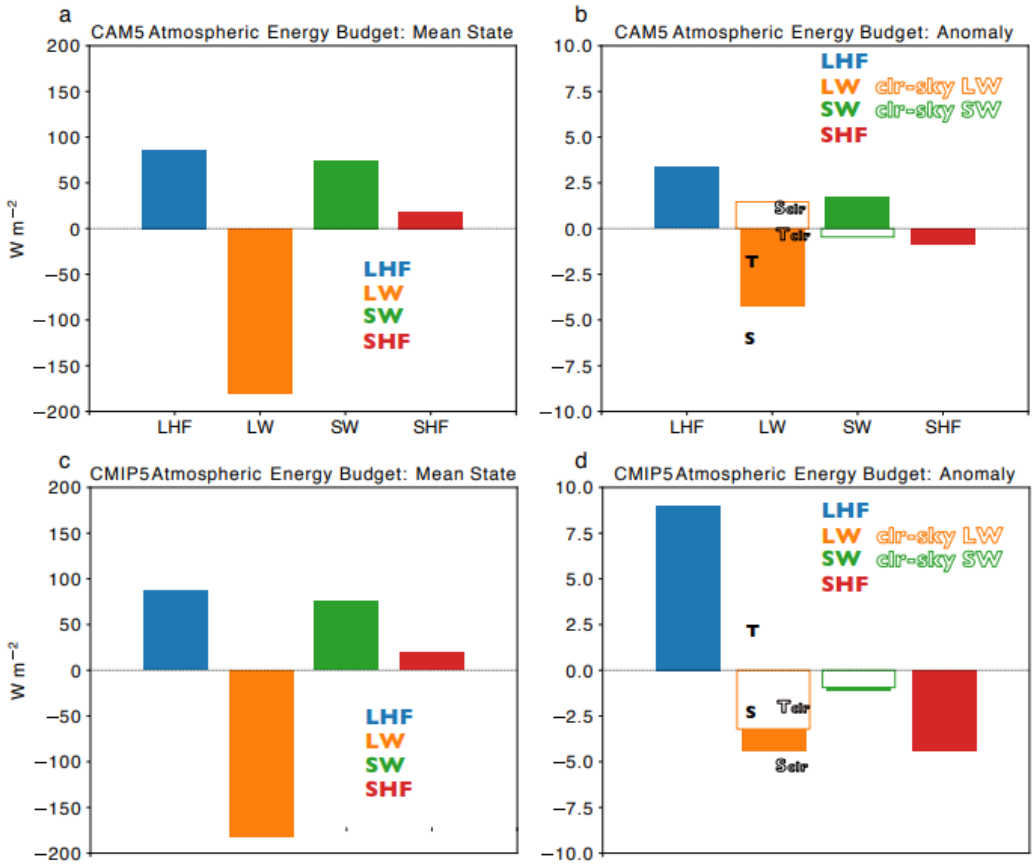

Figure.2 Atmospheric energy budget means and anomalies for the CAM5 experiments and CMIP5 ensemble. a) CAM5 mean atmospheric energy budget. Each bar represents mean la-tent heat flux (blue), all-sky longwave flux (orange), all-sky shortwave flux (green), and sensibleheat flux (red) into the atmosphere. b) Corresponding anomalies between the CAM5 model ex-periments with the highest and lowest global mean precipitation rate. Orange and green edgedbars indicate clear-sky anomalies for longwave and shortwave anomalies. Anomalies of all-skyand clear-sky top-of atmosphere longwave fluxes (T and Tclr) and all-sky and clear-sky surfacelongwave flux anomalies (S and Sclr) are also shown. c) Same as a) but corresponding to CMIP5ensemble means. d) Same as b), but with anomalies between the 5 rainiest models and 5 least-raining models from the CMIP5 ensemble.

12. 热带石笋的 QDM 高分辨率环境磁学研究

翻译人：郑威　11930589@mail.sustech.edu.cn

Fu R R, Hess K, Jaqueto P, et al. ***High-resolution environmental magnetism using the quantum diamond microscope (QDM): Application to a tropical speleothem****[J]. Frontiers in Earth Science, 2021, 8: 674.*

https://doi.org/10.3389/feart.2020.604505

摘要：QDM磁场成像技术是近年来发展起来的一种以1微米分辨率绘制地质样品的磁场源图像的技术。将QDM技术应用于洞穴沉积物可以提供洞穴环境中输入的碎屑的高分辨率时间序列，进而可以获得有用的古环境信息。在这里，我们以年到次年间分辨率绘制了174年时间的巴西中西部洞穴的洞穴沉积物磁场图，并做了剩磁获得实验以量化磁性颗粒种类随时间的变化。我们发现，磁性颗粒高度富集在10-100微米厚的层位中，故对相同的碎屑源进行取样。结合岩相观察和钙镁离子探针图，我们得出，碎屑在样品中富集的原因是由于干燥条件导致的洞穴沉积物生长缓慢或停止。这种解释与氧同位素数据是一致的，说明了洞穴沉积物磁学信息可以用来推断过去发生的干旱，并可能量化其延续的时间。未来对洞穴沉积物的高分辨率磁学成像可能为碎屑富集的机制提供额外的见解，并作为当地湿度和渗透性的代用指标。

ABSTRACT: Quantum diamond microscope (QDM) magnetic field imaging is a recently developed technique capable of mapping magnetic field sources in geologic samples at 1 micrometer resolution. Applying QDM imaging to speleothems can provide high-resolution time series of detrital input into the cave environment, which, in turn, can yield useful paleoenvironmental information. Here we map the magnetic field over a speleothem from midwest Brazil over a 174 year timespan with annual to sub-annual resolution and perform backfield remanence acquisition experiments to quantify changes in the magnetic grain population through time. We find that magnetic particles occur in highly enriched layers of 10–100 μm thickness that sample the same detrital source population. Combined with petrographic observations and electron microprobe mapping of Mg and Ca, we conclude that detrital enrichment in our sample is caused

by drier conditions leading to slow or halted speleothem growth. This interpretation is compatible with oxygen isotopic data and implies that speleothem magnetism can be used to infer the past occurrence of drought and potentially quantify their duration. Future high-resolution magnetic imaging of speleothems may provide additional insight into the mechanism of detrital enrichment and establish their role as a proxy for local moisture and infiltration.

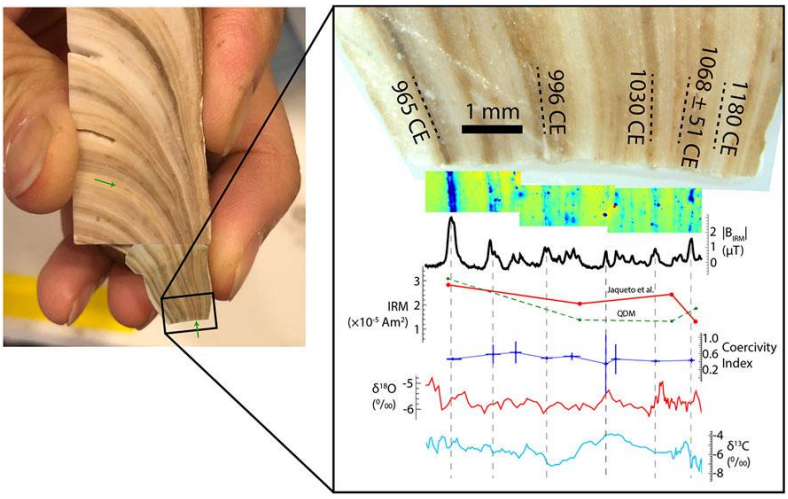

Figure 1. Photographs of the measured sections of the ALHO6 speleothem with age dates, magnetic field time series, and $\delta^{18}O$ and $\delta^{13}C$ data. Age tie point of 1068 CE is based on U-Th dating of laminae while other tie points are interpolated from other U-Th ages based on distances in the speleothem central column. In right panel, first overlay shows the magnetic field map corresponding to a 1.5 T IRM oriented into the mapping plane. BIRM curve is a time series of mean magnetic field intensity computed from the map above. Red and green IRM curves are the bulk samples of Jaqueto et al. (2016) and QDM magnetic field values binned to the same time intervals. Coercivity Index curve is computed for each magnetized band and approximates the fraction of total magnetization with coercivity between 17 and 70 mT. Vertical error bars are 2σ. Oxygen and carbon isotopic data are from Novello et al. (2016). In the left panel, green arrows highlight example of a lamina that shows much stronger coloration in the speleothem flank, although most laminae show greater continuity.

13. 多样品平行 pTRM 差异法测定小高加索地区上新世火山岩古强度，并与 Thellier - Thellier 和 IZZI 法结果比较

翻译人：张伟杰 12031188@mail.sustech.edu.cn

Sánchez M, Elisa M, et al. ***Paleointensity results from Pliocene lavas of the Lesser Caucasus obtained using the multispecimen parallel differential pTRM method: a comparison with Thellier - Thellier and IZZI data****[J].Journal of Geophysical Research: Solid Earth, e2020JB019682.*

https://doi.org/10.1029/2020JB019682

摘要：我们报告了用多样品法（MSP）在 Apnia (Georgia)上新世层序上获得的记录了一次极性反转的古强度结果。利用原始 MSP-DB 和磁畴状态校正 MSP-DSC 协议，对 12 个熔岩流进行了多样品法古强度测定。8 个 MSP-DSC 评估结果通过了选择标准。对比相同熔岩流 MSP 法结果与之前 Thellier-类方法及严格的选择标准得到的古强度结果(Sánchez-Moreno et al., 2020)，根据不同方法的强度值的一致性来获得高可靠的数据。应用多种方法产生了三个新的古强度结果，包括 MSP 和 Thellier-类方法的结果，以及一个额外的由两种不同的 Thellier-类方法得到的结果，其中一个正极性古强度为 36.9 μT 以及三个介于 19.2 μT 和 24.1 μT 反极性结果。此外，本研究用更灵活的标准(TTP)重新解释了 Thellier-类方法的数据，并将结果与 MSP 数据结合起来。最终有 4 个熔岩流通过 MSP 和 Thellier-类方法得到古强度结果，7 个熔岩流通过两种不同的 Thellier-类方法得到古强度结果。正极性段结果为 37.2～44.3 μT，反极性段结果为 12.5～24.6 μT。采用 RCRIT 准则的四个熔岩流的多方法测定结果与同一熔岩流采用 TTP 准则的结果比较，其古强度值及其实验不确定度无显著差异。因此，多方法测定的应用支持了使用 TTP 标准的可行性。

ABSTRACT: We report paleointensity results obtained with the multispecimen method (MSP) over the Pliocene sequence of Apnia (Georgia) which records a polarity reversal. Paleointensity determinations with the multispecimen technique were performed on twelve flows with the original (MSP-DB) and the domain-state corrected (MSP-DSC) protocol. Eight MSP-DSC determinations

passed the proposed quality criteria. To obtain highly reliable data through the agreement between intensity values from different methods, MSP results were combined with paleointensities from a previous study with Thellier-type methods and especially strict selection criteria (RCRIT) on same flows (Sánchez-Moreno et al., 2020). Application of this multimethod procedure resulted in three new paleointensities including both MSP and Thellier-type results and an additional one obtained with two different Thellier-type methods, yielding onepaleointensity of 36.9 μT in the normal-polarity, and three paleointensities between 19.2 and 24.1 μT in the reverse-polarity section. Additionally, Thellier-type data have been reinterpreted in this study with more flexible criteria (TTP) and the results combined with the MSP data. As a result, four flows yield paleointensities including MSP and Thellier-type determinations and seven include paleointensities obtained with two different Thellier-type methods. Results range from 37.2 and 44.3 μT in the normalpolarity and from 12.5 to 24.6 μT in the reverse-polarity section. Comparison of results from the four flows yielding multimethod determinations applying RCRIT criteria with those from the same flows under TTP criteria yields no significant difference in paleointensity values and their experimental uncertainty. Thus, application of a multimethod approach supports the possibility of using TTP criteria.

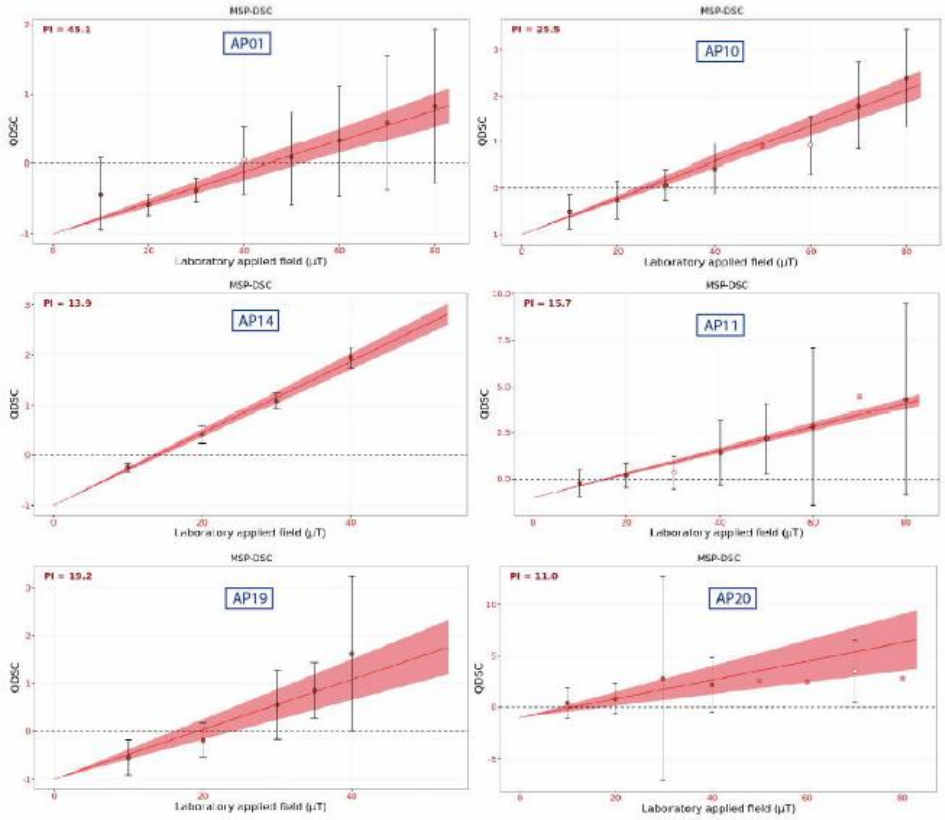

Figure 1. MSP-DSC paleointensity determination plots obtained by the MultiSpecimen Paleointensity on line software (Camps et al., 2016) (http://ambre.gm.univmontp2.fr/camps/MSP_DSC/). AP01, AP10 and AP14 belong to successful determinations, assigned to quality levels of class B, B and A, respectively (see Table 3). AP11, AP19 and AP20 are failed determinations. Their results agree with the Thellier-type ones but show a very low f range in the first two cases or very high ε_{alt} and ΔB values in the case of the latter one (see Table 3). Closed (open) symbols represent data used (rejected) in the paleointensity determination; each of these points is the Q_{DSC} ratio (equation 17 in Fabian and Leonhardt 2010) from each specimen to which a different Blab has been applied; Q_{DSC} vary on function of the α used. The error bar for each point is ΔQi (equation 22 Fabian and Leonhardt, 2010), the absolute error sum of the alteration and correction of the state of domains. The weights are taken as the inverse of the intrinsic errors ΔQi of each measurements. The shaded area (anchored in (0, -1)) is delimited by the CI95 of the best fitting line. For physical reasons, i.e. no pTRM is acquired if a null field is applied during the heating/cooling cycle, the linear fit must be anchored to the intercept (0,-1).

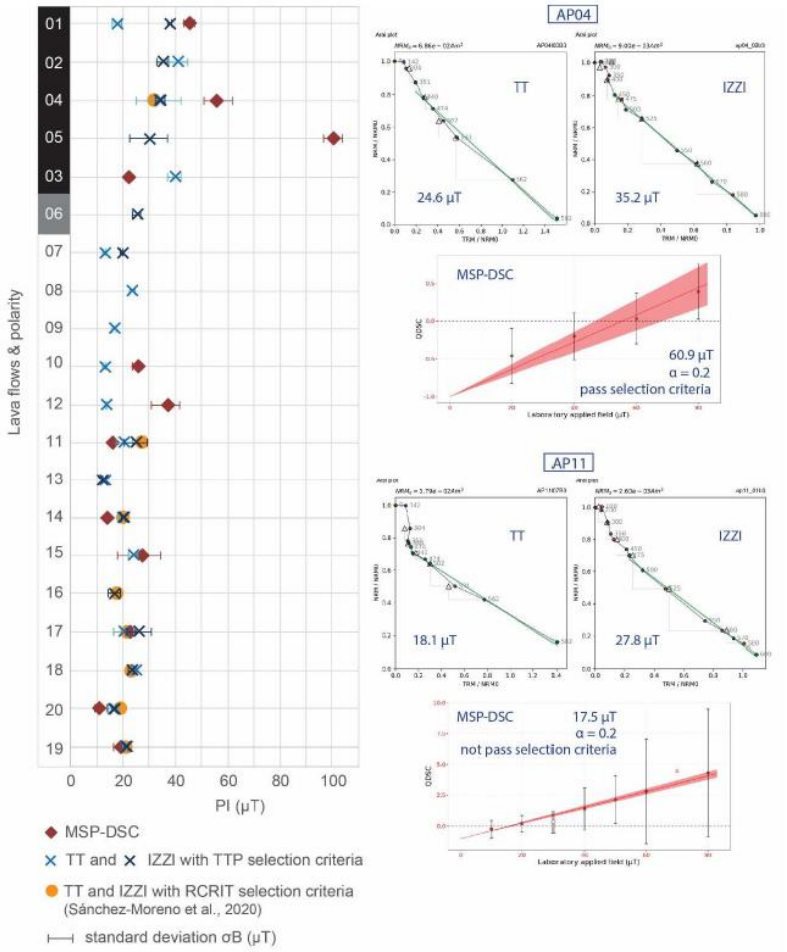

Figure 2. (a) Paleointensities per lava flow obtained in the Apnia sequence by multispecimen with domain-state correction (MSP-DSC) (Fabian and Leonhardt, 2010) and Thellier-Thellier method (TT) (Thellier and Thellier 1959) and IZZI method (Yu et al., 2004) applying TTP (based on Paterson et al., 2014) and RCRIT (Tauxe et al., 2016) selection criteria. MSP-DSC results are plotted whether they pass the proposed selection criteria or not. (b) and (c) Experimental examples from AP04 and AP11 lava flows are shown. TT and IZZI plots interpreted with TTP criteria. MSP plots: closed (open) symbols represent data used (rejected) in the paleointensity determination; each of these points is the Q_{DSC} ratio from each specimen to which a different B_{lab} has been applied; the error bars are the ΔQ_i error; the red line is the linear fit of Q_{DSC} values by weighted minimum squares regression; the shaded area (anchored in (0, -1)) is delimited by 95 % Confidence Intervals (CI_{95}) of the best fitting lines. In the case of AP04, MSP-DSC passes the proposed criteria (Table 3) but the paleointensity value does not match that obtained in the Thellier-type methods. AP11 shows the opposite case, MSP-DSC does not pass the criteria although paleointensities agree.

14. 地球上最深海沟沉积物中微生物碳的高速周转

翻译人：王敦繁 dunfan_w@foxmail.com

Glud R N, Wenzhfer F, Middelboe M, et al. ***High rates of microbial carbon turnover in sediments in the deepest oceanic trench on Earth****[J]. Nature Geoscience,2013,6:284–288.*

https://doi:10.1038/NGEO1773

摘要：微生物控制着海洋沉积物中有机物的分解。反过来，分解有助于海洋养分的再生，并影响有机碳的保存。一般来说，底栖生物的分解速率随水深的增加而下降，尽管深海范围很大，深海沉积物对全球碳循环在数量上是重要的。然而，海洋的最深处实际上仍然没有人探索过。在这里，我们对西太平洋中部马里亚纳海沟挑战者深海沉积物中的微生物活动进行了观察，该海沟近 11000 米深，代表了地球上最深的海沟。我们使用了一个自主研发的微剖面系统来评估海底氧气消耗率。我们的研究表明，尽管大型动物在挑战者深度的存在受到限制，但微生物消耗氧气的速度很高，比附近 6000 米深度的区域高出两倍。对从这两个地点收集的沉积物的分析显示，海沟更深的沉积物微生物细胞浓度更高。沉积物 ^{210}Pb 剖面分析表明，海沟沉积物沉积量较高。我们得出的结论是，挑战者深海区有机物沉积量的升高，维持了极端压力下微生物活动的增强。

ABSTRACT: Microbes control the decomposition of organic matter in marine sediments. Decomposition, in turn, contributes to oceanic nutrient regeneration and influences the preservation of organic carbon1. Generally, rates of benthic decomposition decline with increasing water depth, although given the vast extent of the abyss, deep-sea sediments are quantitatively important for the global carbon cycle. However, the deepest regions of the ocean have remained virtually unexplored. Here, we present observations of microbial activity in sediments at Challenger Deep in the Mariana Trench in the central west Pacific, which at almost 11,000 m depth represents the deepest oceanic site on Earth. We used an autonomous micro-profiling system to assess benthic oxygen consumption rates. We show that although the presence of macrofauna is restricted at Challenger Deep, rates of biological consumption of oxygen are high, exceeding rates at a nearby 6,000-m-deep site by a factor of two. Consistently, analyses of sediments collected from the two sites reveal higher

concentrations of microbial cells at Challenger Deep. Furthermore, analyses of sediment ^{210}Pb profiles reveal relatively high sediment deposition in the trench. We conclude that the elevated deposition of organic matter at Challenger Deep maintains intensified microbial activity at the extreme pressures that characterize this environment.

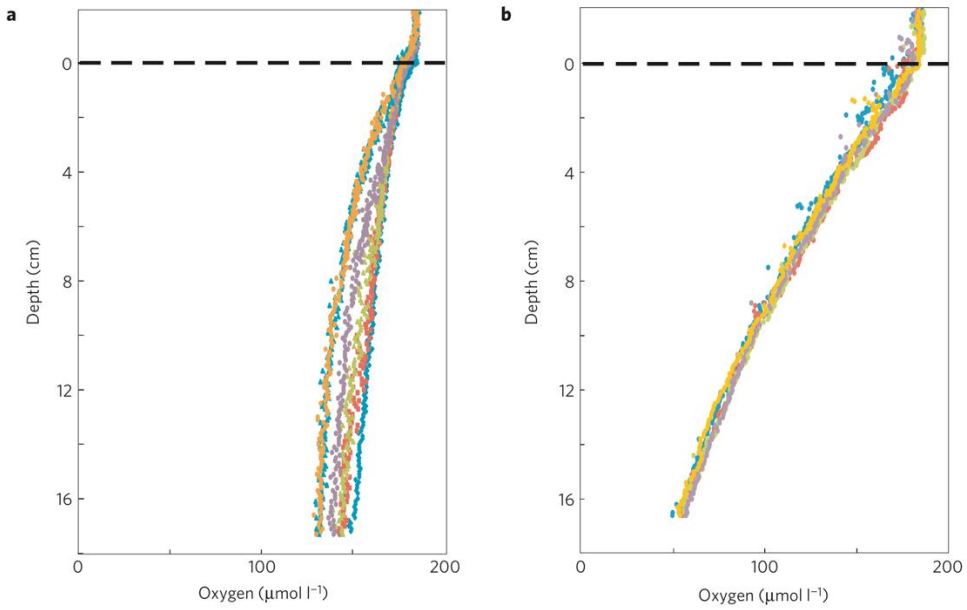

Figure 1: Benthic O_2 distribution measured in situ at the two sites. a, b, O_2 micro-profiles at the reference site (6,018 m water depth; a) and at Challenger Deep (10,817 m water depth; b). Altogether, 36 and 51 micro-profiles were measured at the two sites, respectively. The horizontal dashed line indicates the estimated position of the sediment surface. The faster attenuation in O_2 concentration at the trench site reflects intensified O_2 consumption within the sediment.